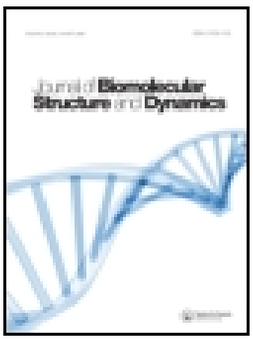

Journal of Biomolecular Structure and Dynamics

ISSN: 0739-1102 (Print) 1538-0254 (Online) Journal homepage: https://www.tandfonline.com/loi/tbsd20

Synthesis, characterization, theoretical, molecular docking and *in vitro* biological activity studies of Ru(II) (η^6-*p*-cymene) complexes with novel aniline substituted aroyl selenoureas

Moideen Musthafa, Ramaiah Konakanchi, Rakesh Ganguly, Chandrasekar Balachandran, Shin Aoki & Anandaram Sreekanth

To cite this article: Moideen Musthafa, Ramaiah Konakanchi, Rakesh Ganguly, Chandrasekar Balachandran, Shin Aoki & Anandaram Sreekanth (2020): Synthesis, characterization, theoretical, molecular docking and *in vitro* biological activity studies of Ru(II) (η^6-*p*-cymene) complexes with novel aniline substituted aroyl selenoureas, Journal of Biomolecular Structure and Dynamics, DOI: 10.1080/07391102.2020.1778531

To link to this article: https://doi.org/10.1080/07391102.2020.1778531

JOURNAL OF BIOMOLECULAR STRUCTURE AND DYNAMICS
https://doi.org/10.1080/07391102.2020.1778531

Taylor & Francis
Taylor & Francis Group

Synthesis, characterization, theoretical, molecular docking and *in vitro* biological activity studies of Ru(II) (η^6-*p*-cymene) complexes with novel aniline substituted aroyl selenoureas

Moideen Musthafa[a], Ramaiah Konakanchi[b], Rakesh Ganguly[c], Chandrasekar Balachandran[d], Shin Aoki[d,e] and Anandaram Sreekanth[a]

[a]Department of Chemistry, National Institute of Technology, Tiruchirappalli, Tamil Nadu, India; [b]Chemistry Division, H&S Department, Malla Reddy Engineering College for Women (Autonomous Institution), Hyderabad, Telangana, India; [c]Division of Chemistry & Biological Chemistry, Nanyang Technological University, Singapore, Singapore; [d]Faculty of Pharmaceutical Sciences, Tokyo University of Science, Noda, Japan; [e]Research Institute for Science and Technology, Tokyo University of Science, Yamazaki, Noda, Japan

Communicated by Ramaswamy H. Sarma

ABSTRACT

A sequence of aroyl selenourea ligands (**L1–L3)** substituted by aniline and their Ru(II) (η^6-*p*-cymene) complexes **(1-3)**, [Ru(II) (η^6-*p*-cymene) L] (L = monodentate aroyl selenourea ligand) have been synthesized and characterized the composition of the ligands and their metal complexes. The molecular structures of ligand **L1** and complex **3** were also confirmed by single XRD crystal method. The single-crystal XRD study showed that aroyl selenourea ligand coordinates with Ru *via* Se novel neutral monodentate atom. *In vitro* DNA interaction studies were investigated by Fluorescence and UV-Visible spectroscopic methods which showed that the intercalative mode of binding is in the order of **1 > 2 > 3** with Ru(II) (η^6-*p*-cymene) complexes. Spectroscopic methods have been used for measuring the binding affinity of bovine serum albumin to complex. Moreover, the cytotoxic study of complexes (**1–3)** were evaluated against HeLa S3, A549, and IMR90 cells, resulting in complexes **1** and **2** showed promising cytotoxic activity against HeLa S3 cell with IC_{50} values of 24 and 26 μM, respectively. Also, the morphological changes of HeLa S3 and A549 cells were confirmed by fluorescence microscope in the presence of complexes **1** and **2** using AO (acridine orange, 200 μM) and EB (ethidium bromide, 100 μM). In addition, the docking results strongly support the protein binding studies of the complexes.

ARTICLE HISTORY
Received 2 April 2020
Accepted 26 May 2020

KEYWORDS
Cytotoxicity; crystal structures; selenourea; Ru(II) (η6-p-cymene; docking studies

1. Introduction

Metal complexes are used to combat cancer and have a massive effect on cancer treatment. According to its specific structure and mechanical growth, magnetic, thermodynamic, intrinsic and kinetic properties, metal complexes are used to produce extremely effective anticancer, DNA and cleaving medicines (Guerriero et al., 2017). Cisplatin has proven to be a drug for anticancer, and several researchers have found other potential metal medicines with increased pharmacological activity since they have high-level neuro, hepato and nephrotoxic side effects (Bruijnincx & Sadler, 2008; Hill & Speer, 1982; Rosenberg, 1978). In order to overcome these problems, scientists concentrated on alternative metal-based bio-compatible medicines (Adeyemo et al., 2018; Muggia, 2009; Swaminathan et al., 2019).

Ruthenium compounds emerged out to be the most promising candidate as anticancer agents. Ruthenium based complexes with a high pharmacological effect are reported to be target-specific and less toxic (Reedijk, 2008; Song et al., 2019). Many ruthenium complexes have been investigated and reported as anticancer agents; ruthenium-arene complexes find their own significance. The main reasons for the increasing design of ruthenium-arene based anticancer drugs are the amphiphilic nature of the arene ruthenium unit, provided by the hydrophobic arene ligand counterbalanced by the hydrophilic metal center, and the synthetic diversity of the arene ligand, which is an excellent framework for the coupling of organic segments for targeted chemotherapy.

Ru-*p*-cymene complexes like [$RuCl_2(\eta^6$-*p*-cymene)(pta)] (RAPTA-C)and [$RuCl_2(\eta^6$-benzene)(pta)] (RAPTA-B) where pta = 1,3,5-triaza-7-phosphaadamantane, have recently attracted considerable attention due to the very promising *in vivo* activities on the inhibition of metastasis growth, together with a high selectivity and low general toxicity. There are also few reports dealing with $RuCl_2(\eta^6$-*p*-cymene) type complexes showing enhanced biological activity on the replacement of pta with other suitable ligand (Figure 1).The structural backbone of the complexes described in this paper is similar to that of RAPTA-C; but pta ligand has been replaced by aroyl selenourea ligand. Moreover, there are a considerable number of reports on the biological applications of [$RuCl_2(\eta^6$-*p*-

CONTACT Anandaram Sreekanth sreekanth@nitt.edu Department of Chemistry, National Institute of Technology, Tiruchirappalli, Tamil Nadu, India
Supplemental data for this article can be accessed online at https://doi.org/10.1080/07391102.2020.1778531

cymene) L] where L is a N or P donor monodentate ligand. Surprisingly, no such complex with Se donor ligand is explored for its biological applications.

Ruthenium based complexes are reported as target-specific and less toxic with high pharmacological effects. In particular, NAMI-A, or trans-[$RuCl_4$(DMSO)(Im)]ImH (where Im is imidazole), is generally nontoxic but is anti-metastatic and prevents cancer spread. KP1019 or trans-[tetrachlorobis(1H-indazole)ruthenate(III)], NKP-1339 or Sodium trans-[tetrachloridobis(1H-indazole)ruthenate(III)], NKP-1339 (IT-139; KP-1339) is the first-in-class ruthenium-based anticancer agent in development against solid cancer with limited side effects. (Bratsos et al., 2007).

In determining the pharmacological properties of complexes, the structure of ligands plays an important key role. Due to the diverse coordination and biological interventions of a wide range, including anticancer, antifungal, anti-tuberculosis, insecticide and other diseases, we were aiming at working on aroyl selenourea ligands (Alcolea et al., 2016; Barbosa et al., 2018; Campos Jr. et al., 2018; Hussain et al., 2014; Musthafa et al., 2019; Olsen et al., 2016). Selenium is known primarily for its antioxidant function and its healing, chemopreventive, anti-inflammatory, and anti-virus properties (Ganther, 1999; Holben & Smith, 1999). Recently, selenoureas have emerged as free radical scavengers, enzyme inhibitors, anticancer agents with biological aspects. (Alcolea et al., 2016; Hussain et al., 2015; Olsen et al., 2016). We describe the *in vitro* cytotoxicity of Ru *p*-cymene complexes with aroyl selenourea ligands. Our monitoring complexes are identical to the RAPTA-B backbone (Coverdale et al., 2019), with the replacement of pta ligand with aroyl selenourea ligand. In addition, there are only a few Ru *p*-cymene complexes for their action against cancer has been reported and this is the first study evaluated for their biological applications on Ru(II) (η^6-*p*-cymene) complexes which contain aroyl selenourea ligands.

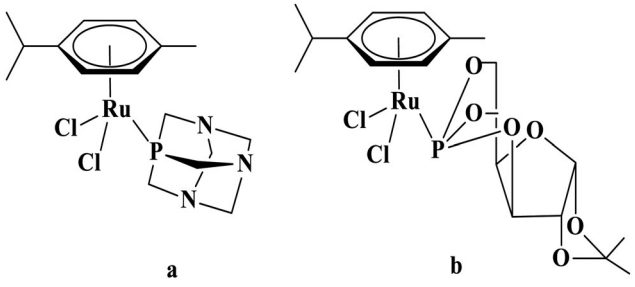

Figure 1. Structure of a) RAPTA-C and b) [$RuCl_2(\eta^6$-*p*-cymene)L] (L = sugar based phosphite analog).

2. Results and discussion

2.1. Synthesis of the ligands and complexes

Benzoyl chloride, or thiophene-2-carbonyl chloride, or furan-2-carbonyl chloride are synthesized as aniline replaced aroyl selenourea ligands (**L1-L3**), potassium selenocyanate, and aniline in dry acetone (Scheme 1) (Musthafa et al., 2020). These aroyl selenourea ligands were allowed to react with the Ru(II) (η^6-*p*-cymene) precursor [$RuCl_2$ (η^6-(*p*-cymene) (**L1-L3**)])]$_2$. In toluene 2:1 molar ratio and the new general formulation complexes, Ru(II) (η^6-*p*-cymene) (L = aniline substituted aroyl selenourea ligands) (Scheme 2) (Jeyalakshmi et al., 2016), high yields are obtained. Elemental analysis, single crystal XRD, UV-Visible, FT-IR, ^{1}H, ^{13}C NMR, and mass spectroscopy experiments are confirming the structures of the ligands and Ru(II) complexes. The complexes are soluble in DMSO, DMF, CH_3OH, $CHCl_3$, and CH_2Cl_2.

2.2. Characterization of the ligands and their complexes

Electronic spectrum of ligands (**L1–L3**) display two strong absorption bands observed approximately at 260–283 and 309–336 nm, respectively, allocated to $\pi \rightarrow \pi^*$ and $n \rightarrow \pi^*$ transitions. Electronic spectra of Ru(II) complexes (**1-3**) were observed at 267–289 nm and according to the selenourea moiety, LMCT bands appear approximately at 334–382 nm. The moderately intense band is assigned to $d \rightarrow d$ transitions in the region of 430–453 nm. The FT-IR spectra of the ligands showed bands in the regions of 3225–3207 cm^{-1} indicate amide N – H, the peak at 3120–3155 cm^{-1} indicate selenourea N – H. The stretching frequencies observed in the range of 1663–1675 cm^{-1} for C = O and 1262–1274 cm^{-1} for C = Se, respectively (Musthafa et al., 2019, 2020). In the complexes N – H and C = O bands remained unchanged, while the ν(C = Se) (1262–1274 cm^{-1}) decreased, indicating that only selenium (neutral monodentate) is coordinated with the Ru ion. The FTIR spectra of ligands and complexes were included in the Supplementary information (SI) (Figures S1–S6). ^{1}H NMR spectra of all the ligands of aroyl selenourea (**L1-L3**) showed that carbonyl and N – H attached selenocarbonyl are observed as singlets and the values appeared in the range of

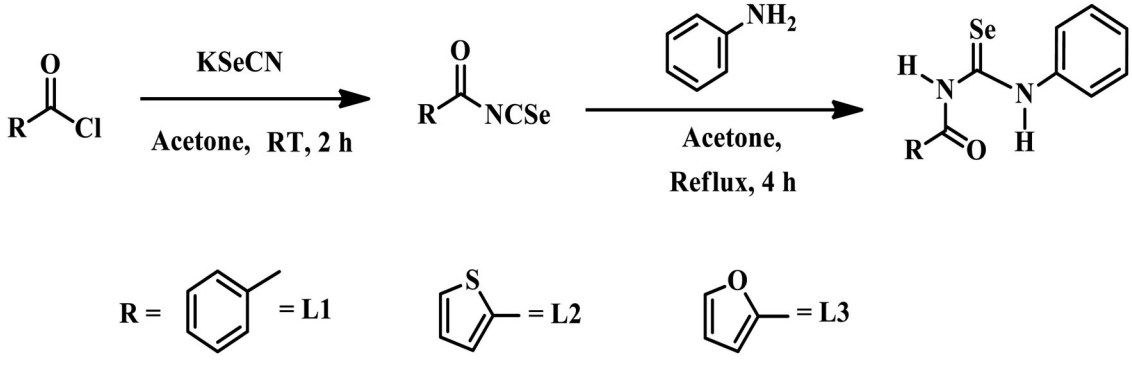

Scheme 1. Synthesis of the aroyl selenourea ligands (**L1-L3**)

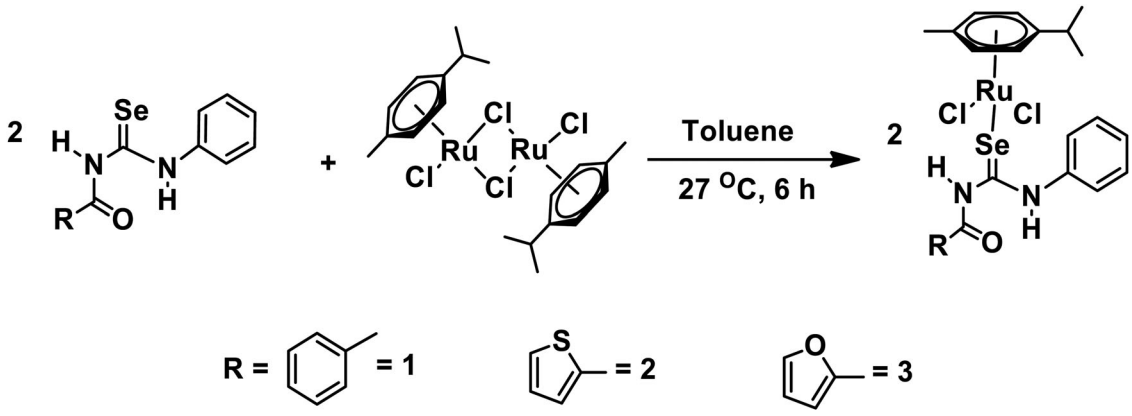

Scheme 2. Synthesis of the $RuCl_2$ (η^6-*p*-cymene) complexes (**1**-**3**)

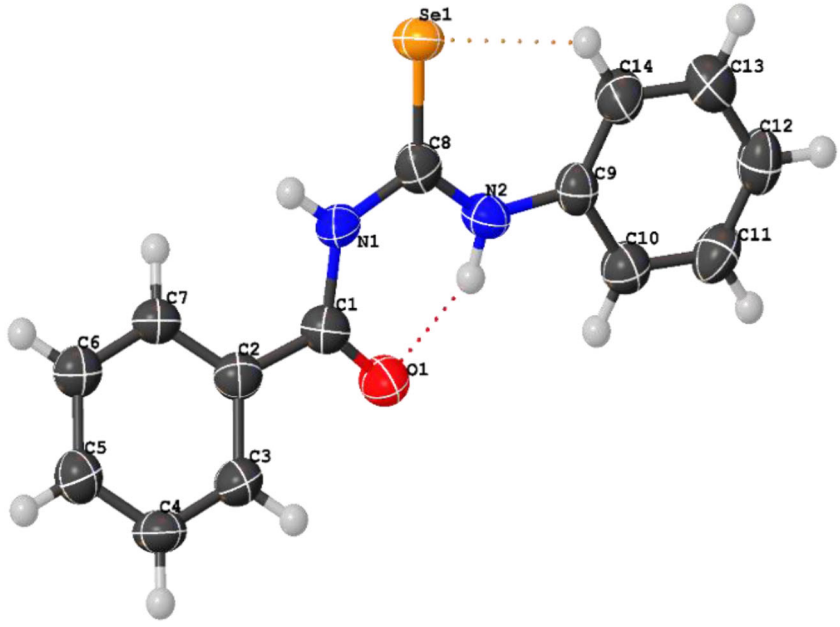

Figure 2. Thermal ellipsoid plot of ligand **L1**.

12.82–13.17 ppm and the peaks at 11.19–11.50 ppm corresponding to selenocarbonyl bound N – H. The signals were observed at 6.55–7.77 ppm indicating all the other aromatic protons (phenyl, thiophene and furan). The ^{13}C NMR spectra of the ligands displayed the signals for C = O and C = Se, respectively at 178.39–178.79 and 158.84–168.67 ppm. Signals were shown to match aromatic carbon in the ligands between 112.0 and 146.1 ppm. The ^{13}C NMR spectra of the complexes showed no significant shifts. The new peaks observed at 79.54–82.33 ppm represent the confirmation of *p*-cymene. The ^{1}H and ^{13}C NMR spectra of the ligands and their metal complexes were shown in the SI (Figures S7–S18) (Jeyalakshmi et al., 2016). The mass spectra of the ligands and their complexes were also confirming the structure of the compounds (Shown in ESI Figures S19–S24, Supporting Information).

2.3. X-ray crystallographic analysis

The ligand **L1** and complex **3** molecular structures were confirmed by single-crystal X-ray diffraction studies as shown in Figures 2–4, respectively. Crystal and selected inter-atomic bond lengths and bond angles are summarized in Tables 1–3. The ligand **L1** has shown monoclinic crystal system and space group P121/c1, and the complex **3** showed monoclinic crystal system and space group P121/n1. The crystal structures of the ligand and its complex were observed that there is a correlation between selenocarbonyl and carbonyl oxygen with intra-molecular hydrogen. The furan ring was oriented in the structures of complex **3** in two opposite directions. Slightly elongated thermal parameters of the furan groups (C18–C21, S2) indicate that a possible disorder, which was successfully modeled between two positions.

2.4. DNA binding studies

Understanding the binding nature of synthesized complexes (**1-3**) towards DNA is a significant step in the development of the anticancer drug, synthetic restriction enzymes and so forth (Mahadevan & Palaniandavar, 1998; Nikolić et al., 2015; Ramakrishnan & Palaniandavar, 2008). Consequently, the

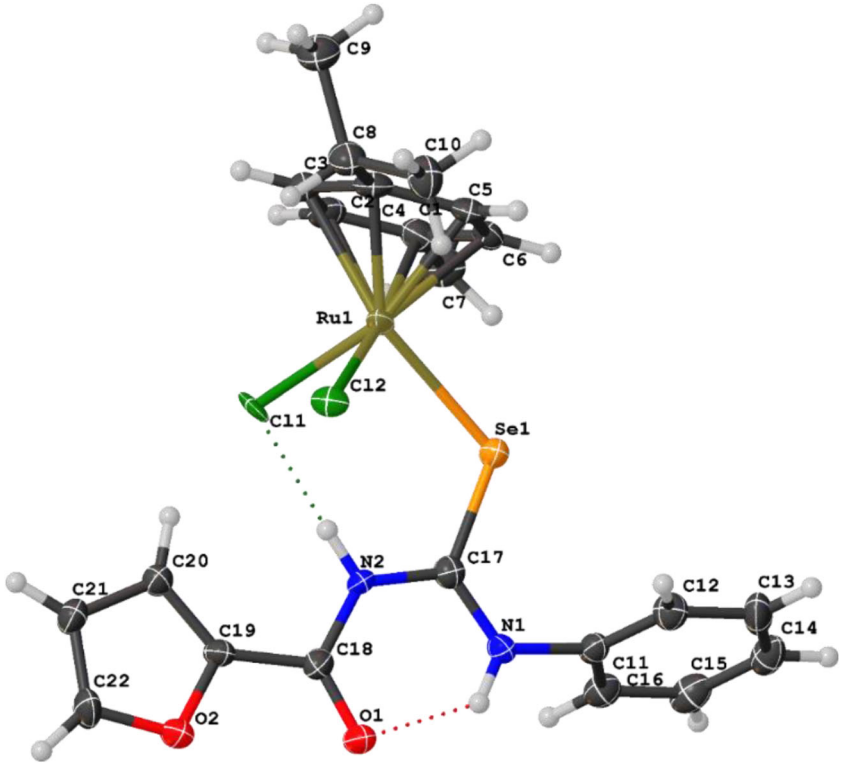

Figure 3. Thermal ellipsoid plot of complex **3** with atomic labeling.

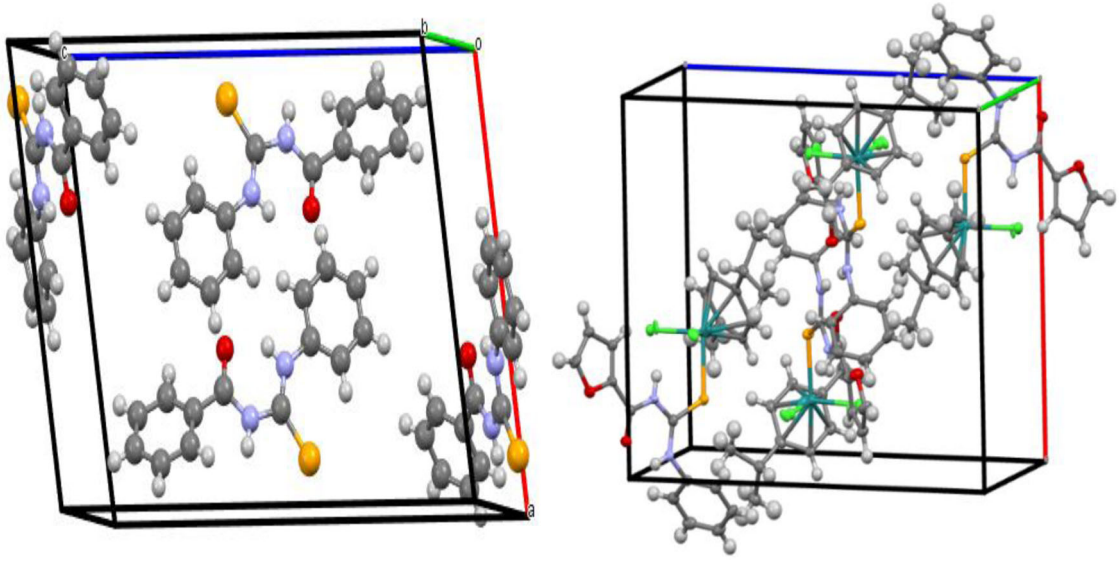

Figure 4. Crystal packing of ligand **L1** and complex **3**.

ability and the trend for the binding of complexes (**1-3**) to CT-DNA were examined with various techniques.

2.4.1. Electronic absorption spectral titration

Electronic spectral experiments have tested the association of complexes (**1-3**) with CT-DNA. Complexes (**1-3**) exhibited a band at 287–320 nm which was used for further studies (Balakrishnan et al., 2019; Jeyalakshmi et al., 2017). It is understood that an intercalated compound bound to DNA demonstrates a hypochromism with a bathochromic difference in the rate of absorption due to the combination of the chromophore with the base DNA pair. The observed spectral changes were plotted by taking [DNA]/($\varepsilon_a-\varepsilon_f$) in Y-axis and [DNA] in X-axis, according to the equation [DNA]/($\varepsilon_a-\varepsilon_f$) = [DNA]/($\varepsilon_b-_{\varepsilon f}$) + 1/$K_b$ ($\varepsilon_b-\varepsilon_f$) where [DNA] is the concentration of DNA in base pairs, ε_a is the apparent extinction coefficient value found by calculating A (observed)/[complex], ε_f is the extinction coefficient for the free compound, and ε_b is the extinction coefficient for the compound in the fully bound form (Rohini, Haribabu, et al., 2018). The intrinsic binding

Table 1. Crystallographic data and refinement parameters for ligand **L1** and complex **3**.

Identification code	L1	3
Empirical formula	$C_{14}H_{12}N_2OSe$	$C_{22}H_{24}Cl_2N_2O_2RuSe$
Formula weight (g/mol)	303.22	599.36
Temperature (K)	100(2)	100(2)
Wavelength (Å)	0.71073	0.71073
Crystal system	Monoclinic	Monoclinic
Space group	P121/c1	P121/n1
Unit cell dimensions		
a (Å)	13.1366(15)	14.3983(5)
b(Å)	4.8877(6)	9.4258(5)
c (Å)	19.895(2)	16.8343(9)
α (°)	90	90
β (°)	103.284(4)	90.7652(15)
γ (°)	90	90
Volume (Å^3)	1243.2(3)	2284.47(19)
Z	4	4
Density (calculated) Mg/m3	1.620	1.743
Absorption coefficient (mm^{-1})	3.008	2.535
F(000)	608	1192
Crystal size (mm^3)	0.040 × 0.060 × 0.220	0.020 × 0.030 × 0.100
Theta range for data collection (°)	2.33 to 27.22°	2.42 to 27.10°
Index ranges	−16 ≤ h ≤ 16, −6 ≤ k ≤ 6, −25 ≤ l ≤ 25	−18 ≤ h ≤ 18, −12 ≤ k ≤12, −18 ≤ l ≤ 21
Reflections collected	15,894	22,874
Independent reflections [R(int)]	2760 0.0841	5021 0.0940
Completeness to theta	99.4	99.7
Absorption correction	Multi-Scan	Multi-Scan
Max. and min. transmission	0.8890 and 0.5570	0.9510 and 0.7860
Refinement method	Full-matrix least-squares on F^2	Full-matrix least-squares on F^2
Data/restraints/parameters	2760/0/163	5021/64/302
Goodness-of-fit on *F*2	1.159	1.020
Final R indices [I > 2sigma(*I*)]	R1 = 0.0471, wR2 = 0.0991	R1 = 0.0411, wR2 = 0.0717
R indices (all data)	R1 = 0.0871, wR2 = 0.1172	R1 = 0.0790, wR2 = 0.0866
Extinction coefficient	n/a	n/a
Largest diff. peak and hole (e.Å^{-3})	0.863 and −0.937	0.743 and −0.862

Table 2. Selected bond lengths (Å) and bond angles (°) for ligand **L1**.

Bond lengths (Å)			
Se1-C8	1.829(5)	C1-O1	1.224(6)
C1-N1	1.390(6)	C8-N2	1.325(6)
C8-N1	1.403(6)	C9-N2	1.407(7)
Bond angles (°)			
O1-C1-N1	122.3(5)	O1-C1-C2	121.4(5)
N1-C1-C2	116.2(4)	N2-C8-N1	114.9(4)
N2-C8-Se1	128.6(4)	N1-C8-Se1	116.5(4)
C14-C9-N2	126.5(5)	C10-C9-N2	113.9(5)
C1-N1-C8	127.2(4)	C8-N2-C9	133.6(4)

Table 3. Selected bond lengths (Å) and bond angles (°) for complex **3**.

Bond lengths (Å)			
Ru1-C1	2.188(5)	Ru1-C2	2.148(5)
Ru1-C3	2.178(4)	Ru1-C4	2.225(5)
Ru1-C5	2.199(5)	Ru1-C6	2.143(5)
Ru1-Cl1	2.431(3)	Ru1-Cl2	2.428(3)
Ru1-Se1	2.5275(13)	C11-N1	1.449(5)
Se1-C17	1.858(5)	C18-N2	1.376(6)
C18-O1	1.219(5)		
Bond angles (°)			
C1-Ru1-Se1	95.30(14)	C2-Ru1-Se1	129.76(16)
C3-Ru1-Se1	161.84(14)	C4-Ru1-Se1	136.10(15)
C5-Ru1-Se1	99.80(13)	C6-Ru1-Se1	82.42(12)
Cl1-Ru1-Se1	91.84(12)	Cl2-Ru1-Se1	91.33(14)
N1-C17-Se1	121.4(3)	N2-C17-Se1	120.0(3)

constant K_b was calculated from the ratio of the slope and the intercept (Aneesrahman et al., 2018). In all the cases, similar trends were observed as can be seen from Figures 5(a) and S25 (Supporting Information). Among the complexes, complex **1** exhibits a maximum shift. Figure 5(b) shows the magnitudes of binding constants (K_b) and the values are tabulated in Table 4. The K_b values were found to be in the range of 5.718×10^5 – 3.991×10^5 M^{-1}. The binding energy of complex **1** is more than that of complex **2** and **3** comparatively. Binding constant values of complex **1** when studied by molecular docking (1BNA) is more than the other 2 complexes (**2** and **3**) (Pursuwani et al., 2020).

2.4.2. Fluorescence spectroscopic studies

Fluorescence spectroscopy was used for further confirmation of the binding modes of the complexes (**1-3**) to DNA. Since all the complexes (**1-3**) did not show any fluorescence in solution, the Ethidium bromide was used as a fluorescence probe (Rohini, Ramaiahet al., 2018). In the Tris buffer solution at room temperature, EB shows a weak luminescence, but in the presence of CT-DNA, the rapid intercalation of DNA base pairs has shown strong luminescence. If the complex under investigation has the intercalation abilities, the intensity of fluorescence starts to decrease as it replaces the EB from

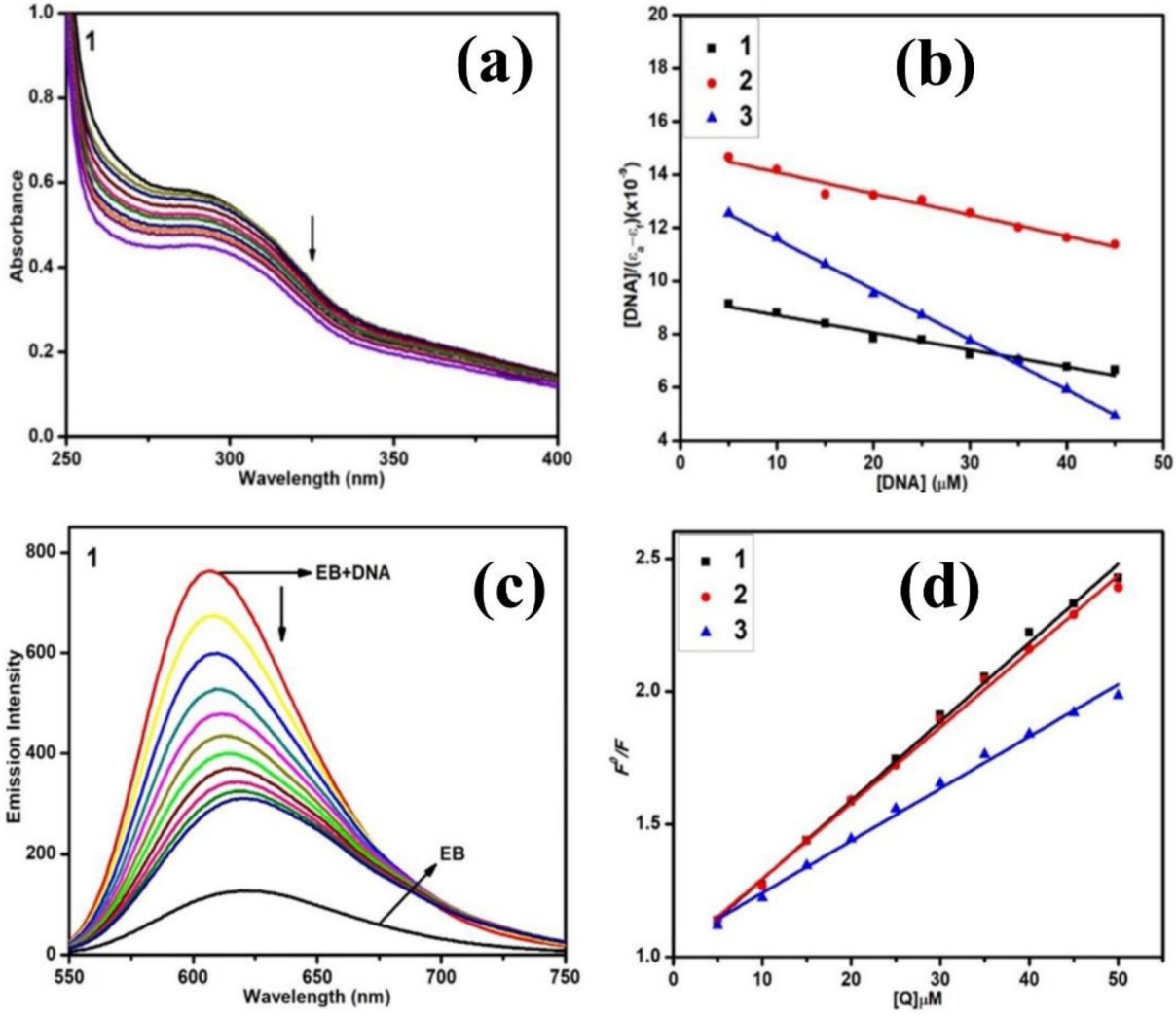

Figure 5. (a) Complex **1** absorption spectra in the Tris-HCl buffer with CT-DNA addition, [DNA] = 0-40 μM, [complex] = 25 μM.The arrow indicates that as the CT-DNA concentration increases the absorption intensity decreases. (b) The plot of titrating complexes with CT-DNA [DNA]/($\varepsilon_a - \varepsilon_f$) *versus* [DNA]. (c) In the presence of complex **1** fluorescence curves EB bound with DNA. [DNA] = 5 μM, [EB] = 5 μM and [complex] = 0–50 μM. (d) The fluorescence titrations of the complexes with CT-DNA are from Stern-Volmer equation.

Table 4. Binding constant of DNA (K_b), Stern-volumer constant (K_q) and apparent binding constant (K_{app}) values of complexes **(1-3)**.

Complex	K_b (M^{-1})	ΔG° (kJ mol^{-1})	K_q (M^{-1})	K_{app} (M^{-1})
1	$5.718 \times 10^5 \pm 0.09$	−27.32	$1.956 \times 10^4 \pm 0.03$	$1.310 \times 10^6 \pm 0.05$
2	$4.811 \times 10^5 \pm 0.06$	−26.89	$1.845 \times 10^4 \pm 0.04$	$1.210 \times 10^6 \pm 0.03$
3	$3.991 \times 10^5 \pm 0.03$	−26.42	$1.883 \times 10^4 \pm 0.08$	$1.110 \times 10^6 \pm 0.02$

DNA, the EB displacement assay, thereby providing indirect proof for the DNA binding mode. In addition to the CT-DNA-EB solution with complexes (**1-3**) (0–50 μM), a decrease in fluorescence intensity was observed up to 59.4, 55.4, and 54.3% with a small redshift (8, 3, and 2 nm) (Figure 4(c) and S26, Supporting Information). The quantitative assessment of the interaction of the complexes with CT DNA was given by Stern-Volmer equation, $Fo/F = 1 + K_q$ [Q] where F^o and F are the fluorescence intensities in the absence and presence of complex respectively, K_q is a linear Stern-Volmer quenching constant, and [Q] is the concentration of complex. The slope of the plot of F^o/F *versus* [Q] gave K_q (Figure 5(c,d)). The apparent DNA binding constant (K_{app}) values were calculated by using the equation K_{EB} [EB] = K_{app} [complex], where [complex] is the complex concentration at 50% reduction in the fluorescence intensity of EB (Muralisankar et al., 2016). The K_q and K_{app} quenching constant is **1** > **2** > **3**, as described in Table 4. The free energies of complexes **1**, **2**, and **3** were evaluated as negative values and are −27.32, −26.89, and −26.42 kJ mol^{-1}. These values indicate that these complexes with DNA interaction spontaneity.

2.5. Protein interaction studies

2.5.1. UV-Visible absorption spectra

In order to determine the quenching mechanism, the BSA UV-Visible absorption spectrum in the presence and absence of complexes **(1-3)** were studied. Quenching usually occurs either by dynamic or static mode. Dynamic quenching is a process in which the fluorophore and the quencher come

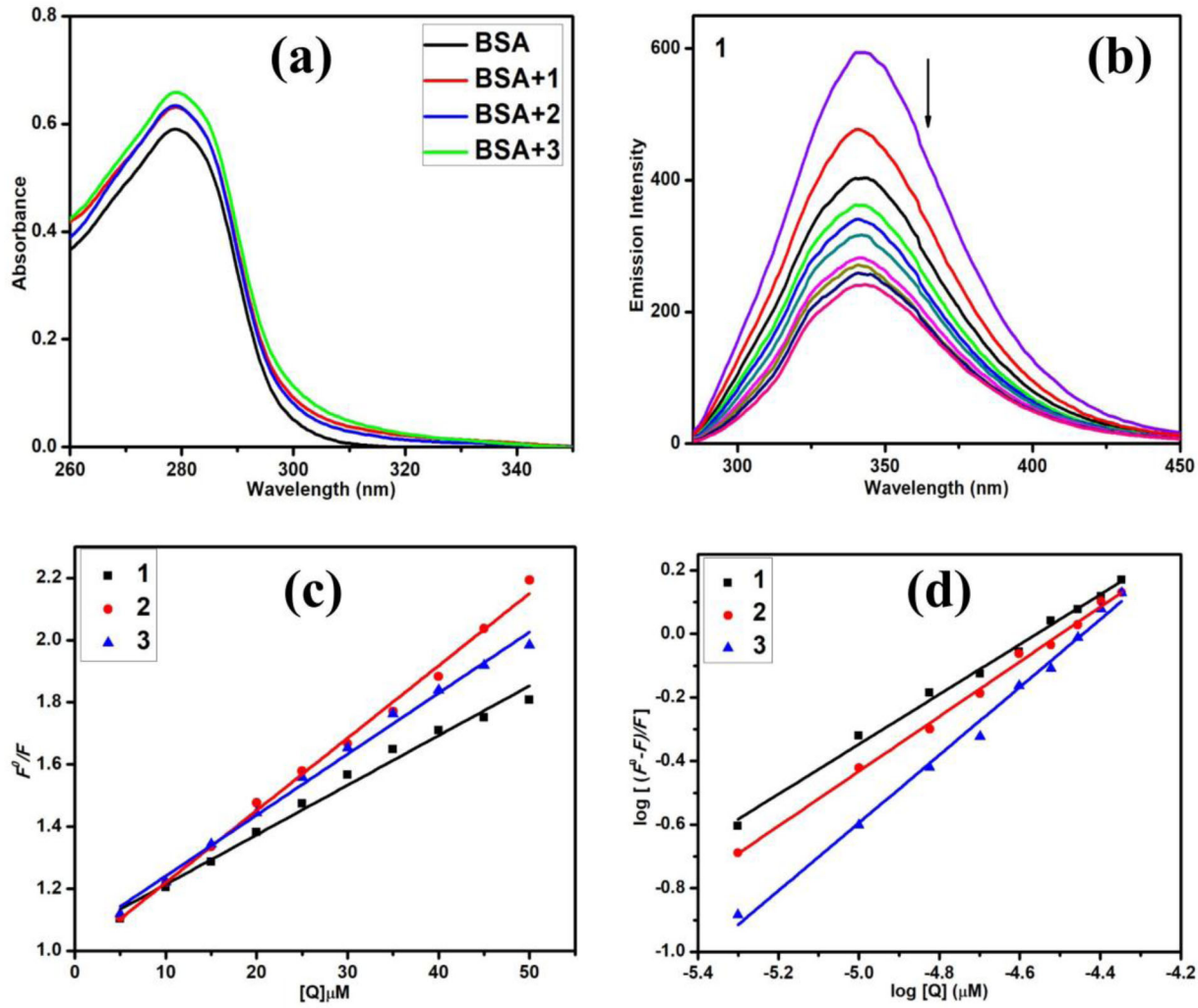

Figure 6. (a) BSA (10 μM) and complexes (**1-3**) (4 μM) BSA absorption spectra, (b) In the absence and presence of complex **1** fluorescence quenching curves of BSA. [BSA] = 1 μM and [complex] = 0–20 μM. (c) The Stern-Volmer diagram of the titrations of fluorescent complexes to BSA. (d) Fluorescence titration of complexes with BSA from Scatchard equation.

into contact during the transient existence in the excited state. On the other hand, static quenching refers to the formation of a fluorophore-quencher complex in the ground state. UV-Visible absorption spectroscopy is the tool to determine the type of quenching involved. The addition of the complexes to BSA leads to an increase in BSA absorption intensity without affecting the position of the absorption band (Figure 6(a)). It showed the existence of static interaction between BSA and the complexes (**1-3**). The complexes (**1-3**) indicated a static type of quenching mechanism as reported (Krishnamoorthy et al., 2012; Lakowicz & Weber, 1973; Ramachandran et al., 2012; Sathyadevi et al., 2012).

2.5.2. Fluorescence spectra

Protein fluorescent properties are largely attributable to residual tryptophan, tyrosine and phenylalanine. Fluorescence changes reflect conformational changes in the protein (Burstein et al., 1973; Mukhopadhyay et al., 2015; Selvakumaran et al., 2014). The interactions of BSA (bovine serum albumin) with complexes (**1–3**) were studied using fluorescent spectroscopy. BSA solution (1 μM) with complexes (**1–3**) (0–20 μM) and changes in fluorescence spectra in 290–500 nm (λ_{ex} 280 nm, Figure 6(b) and S26, Supporting Information) were reported. A fluorescence intensity reduction of BSA was due to the addition complexes (**1–3**) (74.6%, 2 nm, complex **1**; 75.2%, 1 nm, complex **2**; 69.5%, 1 nm, complex **3**, respectively).

The quenching of BSA during the addition of complexes (**1-3**) indicates the interaction of the molecules and the consequent conformational changes. Figure 6(c,d) have measured the binding constant and number of binding sites. Table 5 shows the results of K_q, K_b, and n. The K_q values of complexes (**1–3**) showed a higher binding potential with BSA in complex **2**. The binding sequence observed is **1** > **2** > **3**. From the Scatchard equation, n values obtained for all molecules were ~1, which suggests that the number of binding sites of BSA for each molecule is one. The K_b values also reflect the higher binding potential of complex **1**, compared with BSA complexes **2** and **3**. The free energies of complexes **1**, **2**, and **3** were evaluated as negative values and are −27.42, −26.96, and −25.70 kJ mol^{-1}. These values indicate complexes with BSA interaction spontaneity.

2.6. Frontier molecular analysis (FMO) and molecular electrostatic surfaces (MESP)

2.6.1. FMO analysis

FMO helps to identify electronic transitions and kinetic stability, electric and optical characteristics (Bhat et al., 2019; Li et al., 2013; Konakanchi et al., 2019). FMOs were determined by using BL3YP; LANL2DZ theory rate of all three complexes (**1–3**) as shown in Figure 7. The HOMO-LUMO energy gap of complexes (**1–3**) are 3.03, 3.02, 2.98 eV, respectively (Table S1, Supporting Information). The small difference in the HOMO–LUMO energies of the complexes depicts their similar reactivity nature. In order to assess the important chemical reactivity descriptors such as softness, hardness, electro negativity, chemical potential, and electrostatic and ionization energy, this HOMO–LUMO energy gap was investigated.

Chemical hardness (η) and softness is basically the measurement of chemical reactivity which stabilizes the system and chemical potential μ by applying a charge which gives an idea about the transfer of charge from higher to lower potential (Figure 7). HOMO–LUMO energy of the complexes (**1–3**) are simulated by using theory level BL3YP/LANL2DZ (Bhat Lone, Ali, et al.,2018,; Bhat, Lone, & Srivastava, 2018). Electro negativity (χ) represents the tendency to attract electrons. These properties have been defined as follows:

$$\eta = (\mathrm{I} - \mathrm{A})/2\ \mu = -(\mathrm{I} - \mathrm{A})/2\ \chi = (\mathrm{I} + \mathrm{A})/2$$

In which I and A represents the ionizing potential and electron affinity of the complexes obtained by HOMO and LUMO energies in the form of $I = -E_{HOMO}$ and $A = -E_{LUMO}$ by Janak theorem and Perdew et al. With the use of these equations these descriptors were calculated. It has been observed that the hardness (η) is directly associated with stability is 1.76, 1.66 1.76 e.V for complexes (**1–3**), respectively. The chemical potential μ is primarily the tendency of the electrons to escape from an equilibrium system and it was found to be –3.36, –3.64, and –3.52 for complexes (**1–3**), respectively.

The global index of electrophilicity (ω) is related to the chemical hardness and chemical potential and initially developed by Parr et al. This represents the measure of energy stabilization achieved when an electronic charge from the environment is obtained from the system and is given by the $\omega = \mu^2/\eta$. For complexes (**1–3**), corresponding values are 6.39, 7.98, 7.04 e.V. All of this was measured using BL3YP/LANL2DZ basis set for the target complexes and is shown in Table S1 (Supporting Information). From Table S1 (Supporting Information), it is clear that the energy gap of HOMO–LUMO

Table 5. Constant Protein Binding (K_b), Constant Stern-Volumer (K_q) and number of binding sites (n) values of complexes (**1–3**).

Complex	K_b (M^{-1})	ΔG° (kJ mol^{-1})	K_q (M^{-1})	n
1	$5.966 \times 10^4 \pm 0.04$	–27.42	$7.864 \times 10^4 \pm 0.09$	0.945
2	$4.956 \times 10^4 \pm 0.06$	–26.96	$4.988 \times 10^4 \pm 0.04$	0.923
3	$2.989 \times 10^4 \pm 0.07$	–25.70	$3.711 \times 10^4 \pm 0.07$	0.977

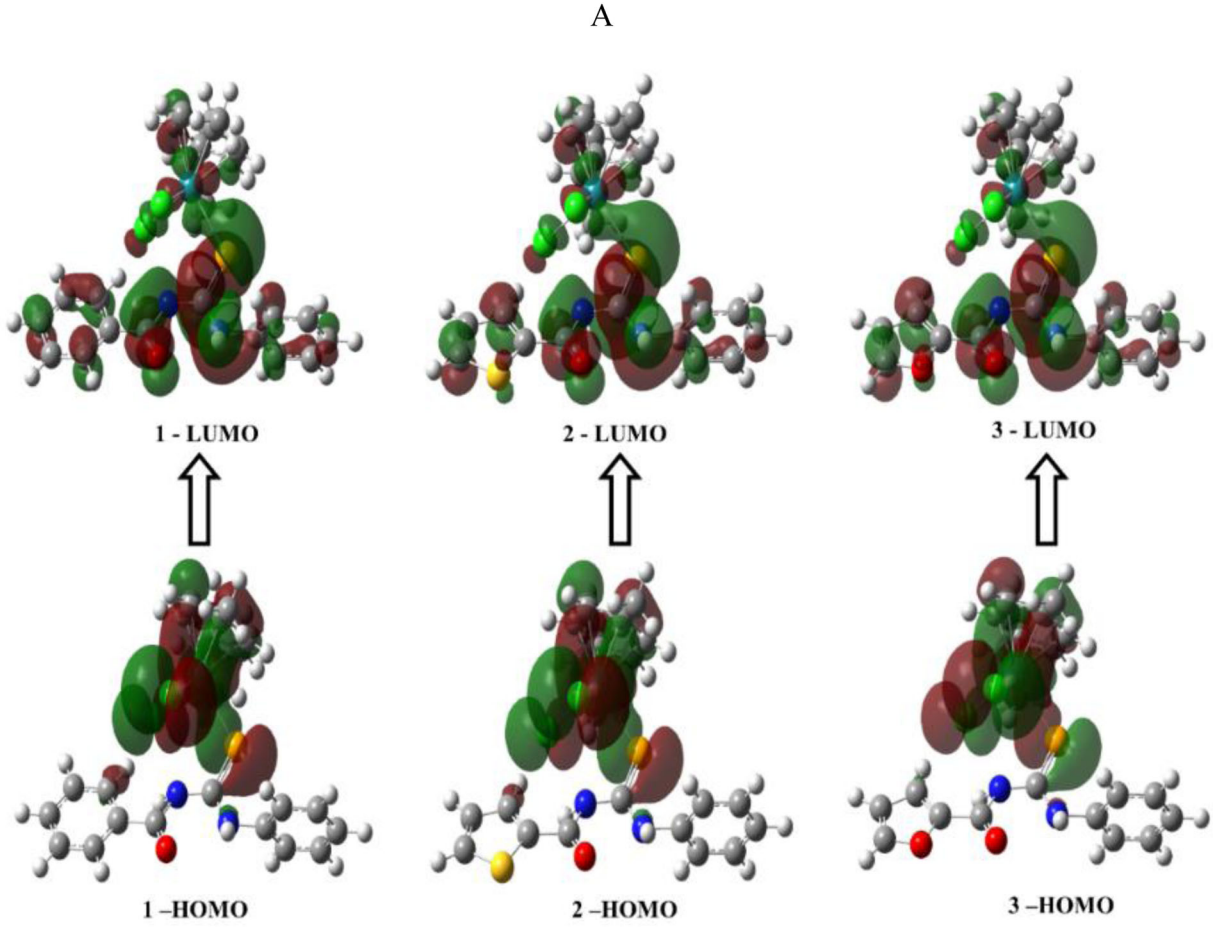

Figure 7. The energy level complexes (**1-3**) of HOMO and LUMO of complexes simulated by DFT; theory level BL3YP/LANL2DZ.

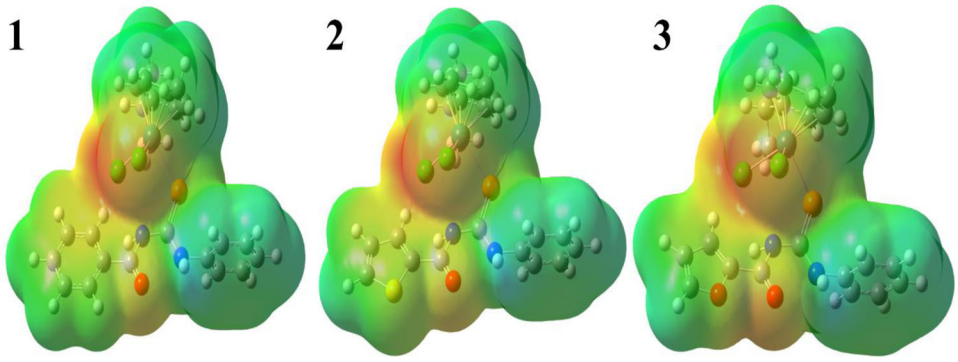

Figure 8. The molecular electrostatic surfaces of complexes (**1–3**).

Table 6. Molecular docking parameters (B-DNA) of complexes (**1-3**).

Complex	No. of rotational bonds	Binding constant of DNA (K_b)	Best binding energy (kcal/mol)	Nucleotide residues involved in the interaction with complexes
1	9	$5.718 \times 10^4 \pm 0.09$	–4.15	DA 17, DA 18
2	9	$4.811 \times 10^4 \pm 0.06$	–4.00	DT 7, DA 18
3	9	$3.991 \times 10^4 \pm 0.03$	–3.04	DG 4, DA 5, DA 17

and reactivity descriptors like hardness, potential and global electrophilicity of each three complexes is more or less similar, suggesting their almost similar behavior in the study of the interaction between enzymes and proteins.

2.6.2. MESP analysis

This is important to predict measures of molecular reactions (Costa et al., 2017; Lone et al., 2018; Ramaiah, Srishailam, et al., 2019). The molecular reactivity to charged reactants is measured and hydrogen binding interactions are shown. The molecular electrostatic surfaces show fundamental properties, such as electron density scale, shape and variance, while correlating them with dipole moment, partial charges, electro negativity and chemical reactivity in the molecule (Ramaiah et al., 2020). MESP for analysis of drug-receptor and enzyme-substrate interactions together with H-bonding interactions has been studied by the computational organic chemists. A contrasting view of the molecular electrostatic maps is shown in Figure 8. Complexes (**1–3**) MESP determined with the basis set BL3YP; LANL2DZ has a similar or more similar environment. The photo representation of electrostatic potential in the rainbow color scheme is between $-6.138\,e^{-2}$, $+6.138\ e^{-2}$, $-6.315\ e^{-2}$, and $+6.315\ e^{-2}$ between $-6.018\,e^{-2}$ and $+6.108\ e^{-2}$, for complexes (**1-3**), respectively. The brightest red region represents the high electron density region (negative potential), and the darkest blue region shows the weak electron density region (positive potential). The experiments carried out by MESPs have shown the three complexes areas most vulnerable to high electron density electrophilic attack involving carbonyl oxygen.

2.7. Molecular docking study

DNA (PDB ID: 1BNA), BSA (PDB ID: 3V03) and human aromatase enzyme (PDB ID: 3EQM) were subjected to the molecular docking process using AutoDock 4.2 molecular docking software and were displayed with Maestro *Schrödinger* software (Gopalakrishnan et al., 2017; Konakanchi et al., 2018; Lone et al., 2018; Morris et al., 2009).

2.7.1. Molecular docking with DNA

Molecular docking is an important *in-silico* computational tool for the rational design of new chemotherapeutic drugs, which predicts non-covalent interaction between the drug molecules and the nucleic acids of DNA. Confirmations of docked complexes were analyzed in terms of energy (kcal/mol). From the docking scores, the binding energy of the complexes were calculated and details are shown in Table 6. Molecular docking experiment reveals that the docked complexes fit into the DNA comfortably, without disrupting the double-helical structure of DNA, resulting in the binding energy between –3.04 and –4.15 kcal/mol. Nucleotide residues involved in the interaction with complexes (**1-3**) is DA 17, DA 18; DT 7, DA 18 and DG 4, DA 5, DA 17, respectively. Complex **1** showed higher binding energy of –4.15 kcal/mol and binding constant of DNA (K_b) of $5.718 \times 10^4 \pm 0.09$ when compared to complexes **2** and **3**. The molecular docking model with DNA (PDB ID: 1BNA) of complex **1** is shown in Figure 9.

2.7.2. Molecular docking with BSA

The molecular docking technique is an attractive scaffold to understand the ligand-protein interactions which can substantiate the experimental results. Conformations of docked complexes were analyzed in terms of binding energy and hydrophobic interaction between complexes and BSA. The molecular docking experiment reveals that the docked complexes fit into the BSA by Van der Waals interaction. The binding energy of the individual complexes has been tabulated and the highest binding energy for each of the

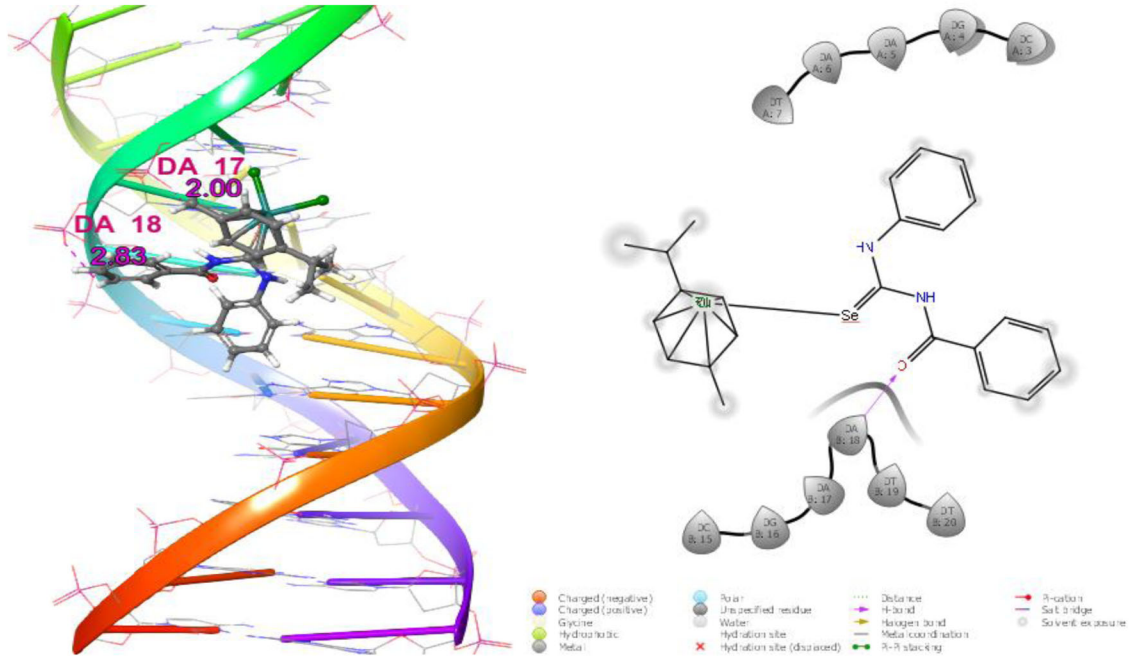

Figure 9. Molecular docking model of complex **1** with DNA (PDB ID: 1BNA).

Table 7. Molecular docking parameters of complexes (**1–3**) with BSA (PDB ID: 3V03).

Complex	No. of Rotational bonds	Number of binding sites (*n*)	Binding constant of BSA (K_b)	Best binding energy (kcal/mol)	Binding forces	Type of binding interaction
1	9	0.945	$5.966 \times 10^4 \pm 0.04$	−12.91	Van der Waals: GLU A:29, LYS A:439, THR A:190, LYS A:294, VAL A:342, ASP A:450, ARG A: A217	Pi-cation: ARG A:194 Mixed pi/alkyl hydrophobic: TYR A:451, CYS A:447
2	9	0.923	$4.956 \times 10^4 \pm 0.06$	−10.48	Van der Waals: HIS A:145, LEU A:189	Pi-Cation: ARG A:458, GLU A:424Pi-Alkyl: LEU A:454, ILE A:455, ALA A:193
3	9	0.977	$2.989 \times 10^4 \pm 0.07$	−3.91	Van der Waals: ILE A:455, ARG A:458	Mixed pi/alkyl hydrophobic: ALA A:193, LEU A:189, HIS A:145 Pi-cation: LYS A:431, LEU A:454

complexes has shown in Table 7. Complex **1** has the highest binding energy and the value of −12.91 kcal/mol and binding constant of BSA (K_b) of $5.966 \times 10^4 \pm 0.04$ when compared to complexes **2** and **3.** Interaction of complex **1** with BSA (PDB ID: 3V03) molecular docked model is shown in Figure 10. The binding force in terms of Van der Waals interactions of complex **1** is GLU A:29, LYS A:439, THR A:190, LYS A:294, VAL A:342, ASP A:450, ARG A: A217, complex **2** is HIS A:145, LEU A:189 and complex **3** is ILE A:455, ARG A:458. Type of binding interaction of complex **1** is pi-cation: ARG A:194 mixed pi/alkyl hydrophobic: TYR A:451, CYS A:447: complex **2** is pi-cation: ARG A:458, GLU A:424 Pi-alkyl: LEU A:454, ILE A:455, ALA A:193 and complex **3** is mixed pi/alkyl hydrophobic: ALA A:193, LEU A:189, HIS A:145 pi-cation: LYS A:431, LEU A:454.

2.7.3. *Molecular docking with the human aromatase enzyme*

All the complexes (**1–3**) were subjected to molecular docking with human aromatase enzyme using the AutoDock Tools (ADT) version 1.5.6 and AutoDock version 4.2 molecular docking software and were displayed with Maestro *Schrödinger* software. The X-ray crystallographic structure of the human aromatase enzyme (PDB ID: 3EQM) was retrieved from Protein Data Bank. Docked ligand conformation was analyzed in terms of energy, hydrogen bonding, and hydrophobic interaction between the ligand and human aromatase enzyme. The binding energy of the individual complexes has been tabulated and the highest binding energy for each of the complexes has shown in Table 8. Complex **1** has the highest binding energy of -6.48 kcal/mol and inhibition constant (K_i) of 38.19 when compared to complexes **2** and **3**. The binding force in terms of Van der Waals interactions of complex **1** is ASN A:571, GLU A:489, GLY A:488, PRO A:666, ASN A:631, ASP A:644, GLY A:490, VAL A:495, ASP A:626, LYS A:517,complex **2** is ASP A:626, PHE A:492, GLY A:490, GLU A:489, ALA A:491, ASN A:571 and complex **3** is GLY A:488, GLY A:490, ASN A:631, LYS A:517, LEU A:633, ASP A:644. Types of binding interaction seen in complexes (**1–3**) are pi-pi interactions, hydrogen bond, pi-cation interaction, pi-alkyl

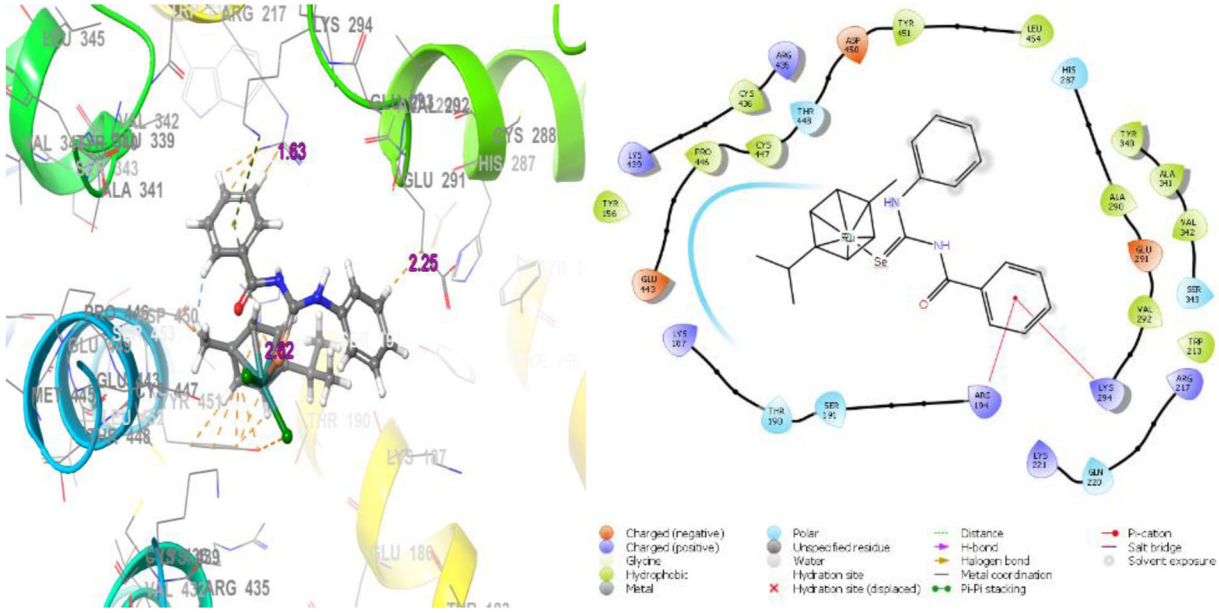

Figure 10. Molecular docking model of complex **1** with BSA (PDB ID: 3V03).

Table 8. Molecular docking parameters of complexes (**1**-**3**) against human aromatase enzyme (PDB ID: 3EQM).

Complex	No. of Rotational bonds	Best binding energy (kcal/mol)	Inhibition constant (K_i) μM	Binding forces	Type of binding interaction
1	9	−6.48	38.19	Van der waals: ASN A:571, GLU A:489, GLY A:488, PRO A:666, ASN A:631, ASP A:644, GLY A:490, VAL A:495, ASP A:626, LYS A:517	Pi-Pi interactions: LEU A:633, ARG A:630 Hydrogen bonds: ALA A:491
2	9	−2.11	15.16	Van der waals: ASP A:626, PHE A:492, GLY A:490, GLU A:489, ALA A:491, ASN A:571	Pi-cation interactions: ARG A:630 Pi-alkyl: PRO A:666
3	9	−1.93	28.33	Van der waals: GLY A:488, GLY A:490, ASN A:631, LYS A:517, LEU A:633, ASP A:644	Mixed pi/alkyl hydrophobic: ARG A:630, PHE A:492, ALA A:491, VAL A:495

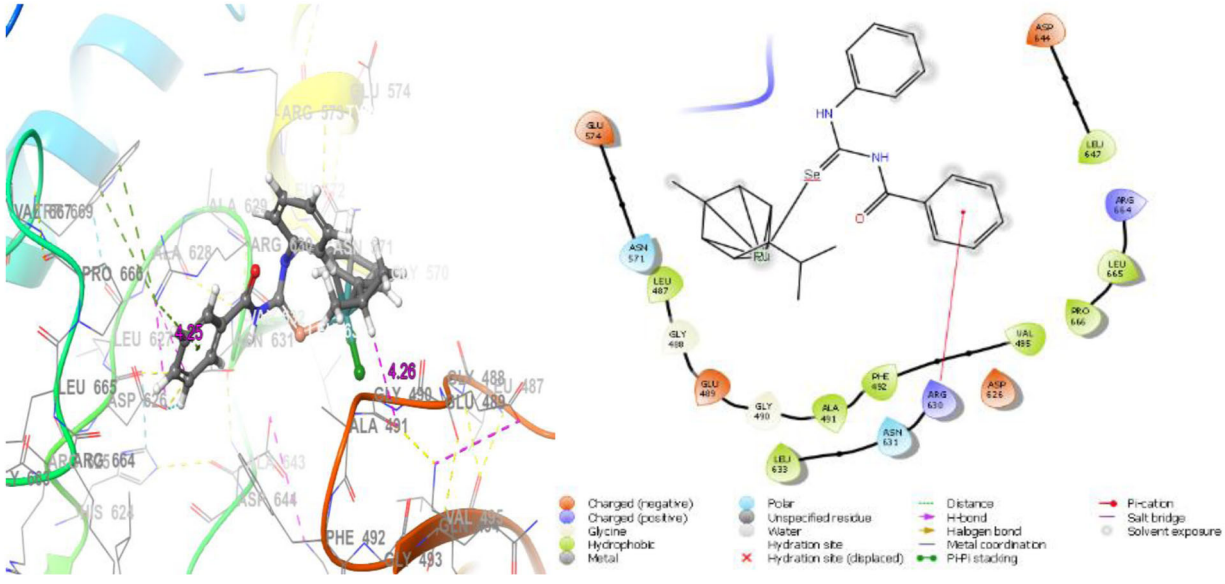

Figure 11. Molecular docking model of complex **1** with human aromatase enzyme (PDB ID: 3EQM).

interaction and mixed pi/alkyl hydrophobic interaction. Complex **1** interaction with BSA (PDB ID: 3V03) molecular docked model is shown in Figure 11.

Based on the docking result of DNA, BSA interaction and *in vitro* experimental studies (Harshitharaj et al., 2016; Kumar et al., 2011), the target molecules were chosen to

demonstrate the effects of the docking parameters (Tables 6–8), and the binding positions were shown in Figures 9–11 and S27–S32 (Supporting Information)). The docking finding showed the higher bonding energy in complex **1** for DNA (–4.65 kcal/mol), BSA (–12.91 kcal/mol), and human aromatase enzyme (–6.48 kcal/mol) than complexes **2** and **3** suggesting enhanced biological activity.

2.8. Cytotoxicity study of complexes (1–3) against HeLa S3, A549, and IMR90 cells

Cytotoxic activity of complexes (**1-3**) were assessed against human cancer HeLa S3, A549, and normal IMR90 cells by MTT assay (Balachandran et al., 2018; Konakanchi et al., 2018; Ramaiah et al., 2019). The cytotoxicity results revealed that complexes **1** and **2** showed promising cytotoxic activity against HeLa S3 cell with 50% inhibition of cell proliferation was observed at 24 and 26 μM, respectively, as summarized in Table 9 and Figure 12. At the same time, complexes **1** and **2** showed moderate cytotoxic activity against A549 cells with 50% inhibition of cell proliferation was observed at 64 and 69 μM, respectively. Moreover, complex **3** showed weak and least cytotoxic activity against both tested HeLa S3 and A549 cells. The cytotoxicity study is then carried out with complexes (**1-3**) against normal IMR90 cells (Table 9 and Figure S33 in the Supporting Information), resulting no toxicity was observed up to 100 μM, suggest that complexes **1** and **2** as a promising anticancer agent against HeLa S3 cells than A549 cells with less toxicity. The Ru-*p*-cymene complexes (**1–3**) showed higher activity than the recently reported ruthenium complexes (Moideen et al., 2020). In addition, the cytotoxic activity also compared with well-known anticancer agent cisplatin.

Table 9. IC_{50} values of complexes (**1-3**) against A549, HeLa S3, and IMR-90 cell lines.

Complex	A549 (μM)	HeLa S3 (μM)	IMR-90 (μM)
1	64	**24**	>100
2	69	**26**	>100
3	83	56	>100
Cisplatin	**23**	**26**	–

2.9. Fluorescence microscopic study of complexes 1 and 2

Morphological changes of HeLa S3 and A549 cells were assessed by a fluorescence microscope in the presence of complexes **1** and **2** using AO (acridine orange, 200 μM) and EB (ethidium bromide, 100 μM) (Jeyalakshmi et al., 2019). AO is an indicator of live cells and EB is an indicator of dead cells. HeLa S3 and A549 cells were treated with complex **1** (50 μM, 100 μM) and complex **2** (50 μM, 100 μM) for 24 h and then co-stained with AO/EB for 15 min at dark condition. The images were taken immediately at the fluorescence microscope (Biorevo, BZ-9000, Keyence). The results revealed that the dramatic morphological changes were observed when the exposure of complexes **1** and **2** in HeLa S3 and A549 cells is summarized in Figures 13 and 14. We speculated that complexes **1** and **2** induce apoptosis mediated cell death in cancer cells.

3. Conclusion

Spectroscopic techniques like FTIR, UV-Visible, ^{1}H, ^{13}C NMR and mass spectra were used to characterize and confirm the structure of aniline substituted aroyl selenourea derivatives. The molecular structures were evaluated using single-crystal X-ray diffraction. Ligand **L1** and complex **3** belongs to monoclinic crystal systems, with space groups P121/c1 and P121/n1, containing four and two molecules per unit cell, respectively. *In vitro* anticancer activity of the complexes **1** and **2** have shown promising activity against HeLa S3 with IC_{50} values of 24 and 26 μM, respectively compared with standard drug cisplatin with IC_{50} value of 24 μM. Finally, these encouraging results are helpful in the *in vivo* biological applications in future endeavors.

4. Experimental

4.1. Synthesis of aniline substituted aroyl selenourea ligands (L1-L3)

The ligands **(L1-L3)** were prepared by the following method. A solution of benzoyl chloride (0.6 mL, 5 mmol) or thiophene-2-carbonyl chloride (0.6 mL, 5 mmol) or furan -2-carbonyl

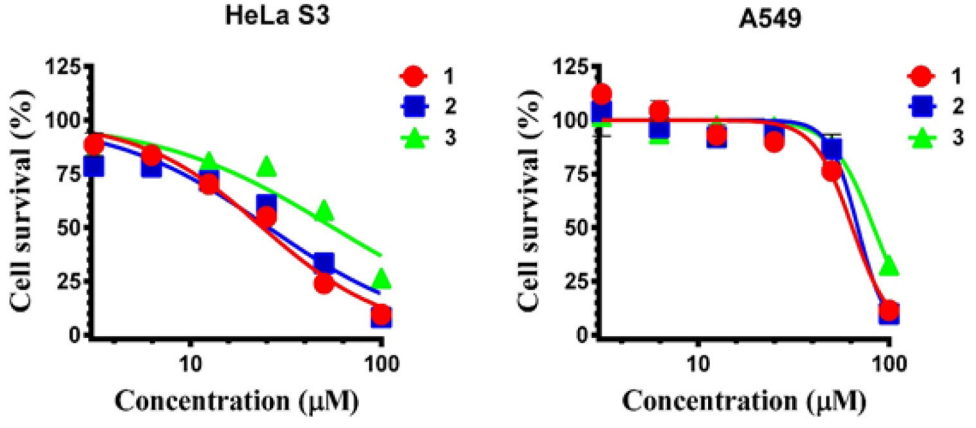

Figure 12. Cytotoxic study of complexes (**1-3**) against HeLa S3 and A549 cells. Three independent experiments were used to measure the results of mean ± SD.

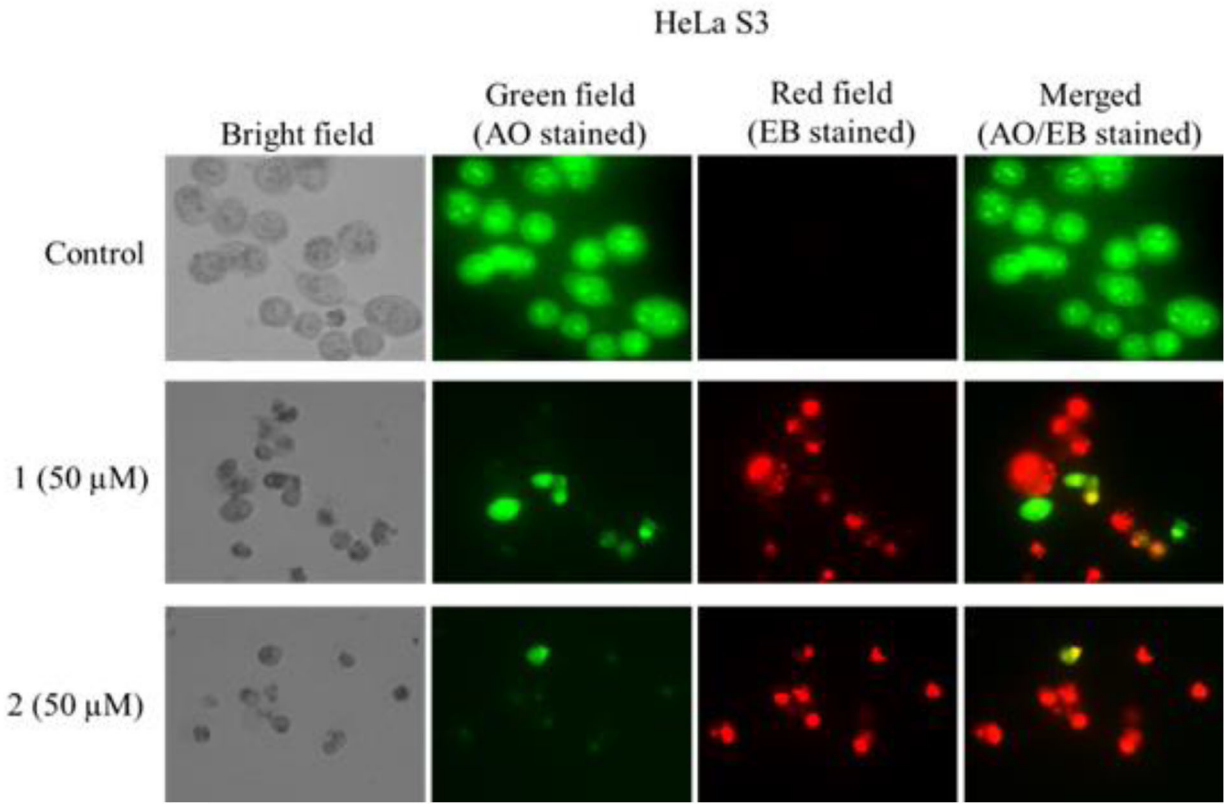

Figure 13. Cancer cell death and morphological changes of HeLa S3 cells were examined by fluorescence microscope (Biorevo, BZ-9000, Keyence, 20×) using fluorescence dyes such as AO (acridine orange, 200 μM) and EB (ethidium bromide, 100 μM) after the treatment of complexes **1** and **2** for 24 h.

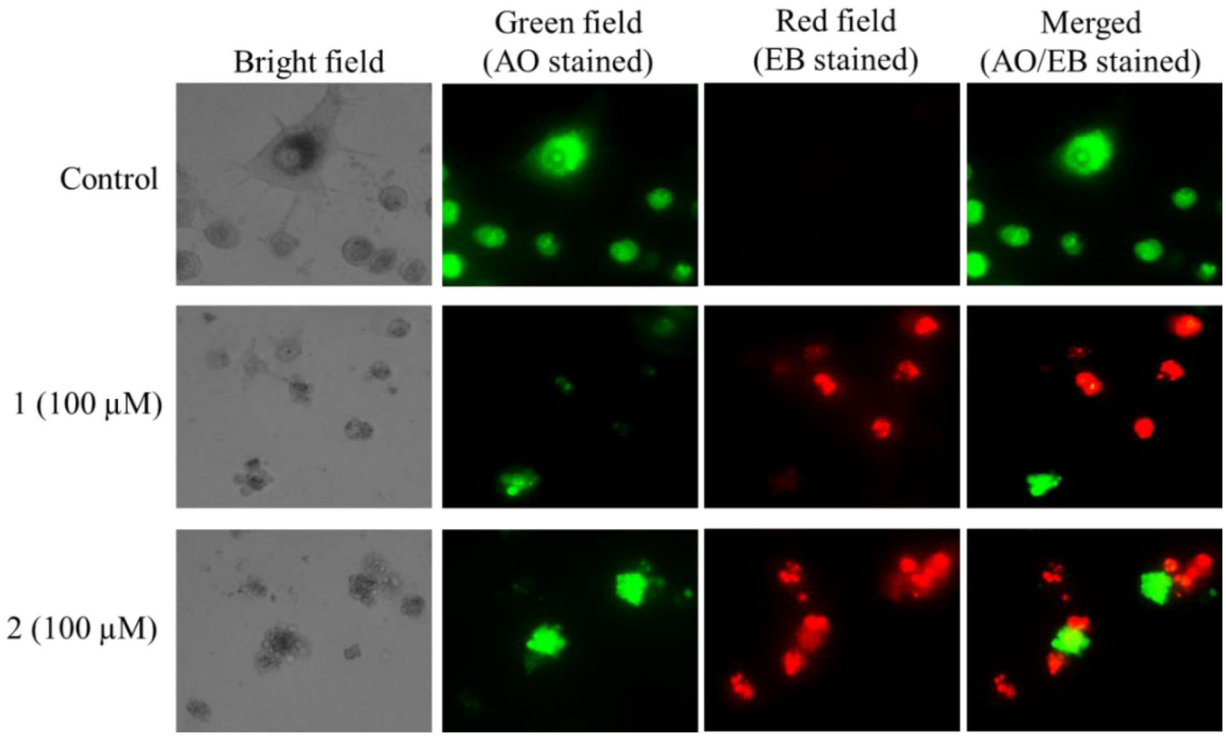

Figure 14. Cancer cell death and morphological changes of A549 cells were examined by fluorescence microscope (Biorevo, BZ-9000, Keyence, 20×) using fluorescence dyes such as AO (acridine orange, 200 μM) and EB (ethidium bromide, 100 μM) after the treatment of complexes **1** and **2** for 24 h.

chloride (0.5 mL, 5 mmol) in dry acetone (25 mL) was added dropwise to potassium selenocyanate (0.485 g, 5 mmol) in dry acetone (25 mL). The reaction mixture was stirred for one hour at room temperature. After cooling, aniline (1 g, 5 mmol) dissolved in acetone (30 mL) was added to it dropwise, and the resulting mixture was refluxed for 2 h at 65 °C.

The reaction mixture was poured into hydrochloric acid (0.1 N, 200 mL) and the resulting pale yellow/brown substance was filtered off. Recrystallisation purified the solid product from a chloroform/ethanol mixture (1/2).

4.1.1 N-(phenylcarbamoselenoyl)benzamide (L1)

Yield: 1.25 g, 74%. Yellow solid, m.p.: 154 °C. Anal. Calc. for $C_{14}H_{12}N_2OSe$ (%): C, 55.46; H, 3.99; N, 9.24. Found: C, 55.38; H, 4.05; N, 9.20. UV–Vis (DMF): λ_{max}, nm 260, 309. FT-IR: υ, cm^{-1} 3344, 3260 (N – H), 3027 (=C – H), 1667 (C = O), 1262 (C = Se). ^{1}H NMR (500 MHz, $CDCl_3$): δ, ppm 12.98 (s, 1H, NH), 11.80 (s, 1H, NH), 8.00-7.98 (d, J = 4 Hz, 2H), 7.69-7.68 (d, J = 4 Hz, 3H), 7.58-7.56 (d, J = 8 Hz, 2H), 7.55-7.47 (t, J = 6 Hz, 2H), 7.45–7.34 (m, 1H). ^{13}C NMR (125 MHz, $CDCl_3$): δ, ppm 180.96 (C = Se), 168.61 (C = O), 139.47, 133.71, 132.43, 129.26, 129.18, 128.92, 127.39, 125.62. LC-MS = 303.02 $[M-H]^-$.

4.1.2 N-(phenylcarbamoselenoyl)thiophene-2-carboxamide (L2)

Yield: 1.30 g, 72%. Yellow solid, m.p.: 160 °C. Anal. Calc. for $C_{21}H_{16}N_2OSeS$ (%): C, 46.61; H, 3.26; N, 9.06; S, 10.37. Found: C, 46.51; H, 3.29; N, 9.04; S, 10.12. UV-Vis (DMF): λ_{max}, nm 276, 314. FT-IR: υ, cm^{-1} 3389, 3270 (N – H), 3069 (=C – H), 1668 (C = O), 1269 (C = Se). ^{1}H NMR (500 MHz, $CDCl_3$): δ, ppm 11.80 (s, 1H, NH), 9.14 (s, 1H, NH), 7.74–7.72 (d, J = 4 Hz, 1H), 7.62–7.60 (d, J = 4 Hz, 1H), 7.48–7.46 (d, J = 8 Hz, 2H), 7.43–7.42 (t, J = 6 Hz, 2H), 7.39–7.21 (m, 2H). ^{13}C NMR (125 MHz, $CDCl_3$): δ, ppm 179.72 (C = Se), 161.11 (C = O), 138.43, 135.62, 134.73, 131.04, 129.06, 128.67, 127.65, 124.72. LC-MS = 308.96 $[M-H]^-$.

4.1.3 N-(phenylcarbamoselenoyl)furan-2-carboxamide (L3)

Yield: 1.06 g, 71%. Pale yellow solid, m.p.: 145 °C. Anal. Calc. for $C_{21}H_{16}N_2O_2Se$ (%): C, 49.01; H, 3.47; N, 9.52. Found: C, 49.82; H, 3.53; N, 9.56; UV–Vis (DMF): λ_{max}, nm 283, 336. FT-IR: υ, cm^{-1} 3275, 3118 (N – H), 3045 (=C – H), 1670 (C = O), 1279 (C = Se). ^{1}H NMR (500 MHz, $CDCl_3$): δ, ppm 12.66 (s, 1H, NH), 9.48 (s, 1H, NH), 7.63–7.62 (d, J = 4 Hz, 1H), 7.58–7.38 (d, J = 4 Hz, 1H), 7.36–7.35 (d, J = 8 Hz, 2H), 7.28–7.27 (t, J = 6 Hz, 2H), 7.25–6.58 (m, 2H). ^{13}C NMR (125 MHz, $CDCl_3$): δ, ppm 179.72 (C = Se), 156.61 (C = O), 146.73, 144.70, 138.47, 129.02, 127.58, 124.69, 119.35, 113.54. LC-MS = 293.05 $[M-H]^-$.

4.2. Synthesis of complexes

4.2.1 [Ru(II)(η^6-p-cymene) L1] (1)

[Ru(II)(η^6-p-cymene)]$_2$ (0.22 g, 0.44 mmol) and L1 (0.326 g, 0.88 mmol) were used. Yield: 71%. Orange solid, m.p.: 206 °C. Anal. Calc. for $C_{29}H_{24}Cl_2N_2ORuSe$: C, 47.30; H, 4.30; N, 4.60. Found: C, 47.15; H, 4.42; N, 4.56. UV–Vis (DMF): λ_{max}, nm 267, 334, 430. FT-IR: υ, cm^{-1} 3207, 3120 (N–H), 3022 (=C–H), 1663 (C = O), 1262 (C = Se). ^{1}H NMR (500 MHz, $CDCl_3$): δ, ppm 13.17 (s, 1H, NH), 11.50 (s, 1H, NH), 8.25–8.24 (d, J = 5.0 Hz, 1H), 7.92–7.84 (d, J = 5.0 Hz, 1H), 7.82–7.61 (m, 4H), 7.39–7.60 (m, 1H), 7.43–7.08 (t, J = 5.0 Hz, 1H), 5.39–5.27 (d, J = 10.0 Hz, 2H, p-cymene phenyl-H), 5.14–5.20 (d, J = 5.0 Hz, 2H, p-cymene phenyl-H), 2.88–2.81 (m, 1H, p-cymene $CH(CH_3)_2$), 2.14 (s, 3H, p-cymene CH_3), 1.82–1.75 (d, J = 10.0 Hz, 6H, p-cymene $CH(CH_3)_2$). ^{13}C NMR (125 MHz, $CDCl_3$): δ, ppm 178.39 (C = Se), 168.67 (C = O), 135.6, 133.5, 133.5, 131.0, 130.9, 129.5, 128.8, 128.4, 128.1, 85.5 (benzene carbon). LC-MS = 611.41 $[M]^+$.

4.2.2 [Ru(II)(η^6-p-cymene) L2] (2)

[$RuCl_2$(η^6- p-cymene)]$_2$ (0.22 g, 0.44 mmol) and L2 (0.317 g, 0.88 mmol) were used. Yield: 83%. Yellowish orange solid, m.p.: 210 °C. Anal. Calc. for $C_{27}H_{22}Cl_2N_2O_2RuSe$: C, 42.93; H, 3.93; N, 4.55; S, 5.21. Found: C, 42.52; H, 3.35; N, 4.44; S, 5.15. UV-Vis (DMF): λ_{max}, nm 275, 347, 436. FT-IR: υ, cm^{-1} 3219, 3155 (N–H), 3155 (=C–H), 1657 (C = O), 1274 (C = Se). ^{1}H NMR (500 MHz, $CDCl_3$): δ, ppm 12.92 (s, 1H, NH), 11.32 (s, 1H, NH), 8.64 (s, 1H), 8.60 (d, J = 8.7 Hz, 2H), 8.01 (s, 1H), 7.97 (dd, J = 14.0, 7.5 Hz, 4H), 7.65 (t, J = 7.4 Hz, 2H), 7.43 (s, 2H), 7.14 (s, 1H), 5.34–5.27 (d, J = 10.0 Hz, 2H, p-cymene phenyl-H), 5.26-5.25 (d, J = 5.0 Hz, 2H, p-cymene phenyl-H), 2.95–2.92 (m, 1H, p-cymene $CH(CH_3)_2$), 2.88 (s, 3H, p-cymene CH_3), 2.23-1.69 (d, J = 10.0 Hz, 6H, p-cymene $CH(CH_3)_2$). ^{13}C NMR (125 MHz, $CDCl_3$): δ, ppm 178.59 (C = Se), 163.52 (C = O), 137.22, 136.42, 135.50, 134.99, 129.37, 128.61, 126.43 (aromatic carbons), 102.83, 83.22, 82.39, 81.33, 80.57 (aromatic carbons of p-cymene), 30.55, 22.30, 18.41 (aliphatic carbons). LC-MS = 616.42 $[M]^+$.

4.2.3 [Ru(II)(η^6-p-cymene) L3] (3)

[$RuCl_2$ (η^6- p-cymene)]$_2$ (0.22 g, 0.44 mmol) and L3 (0.331 g, 0.88 mmol) were used. Yield: 75%. Orange solid, m.p.: 205 °C. Anal. Calc. for $C_{27}H_{22}Cl_2N_2ORuSeS$: C, 44.09; H, 4.04; N, 4.67. Found: C, 43.09; H, 4.08; N, 4.39. UV–Vis (DMF): λ_{max}, nm 287, 382, 453. FT-IR: υ, cm^{-1} 3225, 3149 (N–H), 3040 (=C–H), 1675 (C = O), 1268 (C = Se). ^{1}H NMR (500 MHz, $CDCl_3$): δ, ppm 12.82 (s, 1H, NH), 11.19 (s, 1H, NH), 5.36–5.23 (d, J = 10.0 Hz, 2H, p-cymene phenyl-H), 5.26–5.25 (d, J = 5.0 Hz, 2H, p-cymene phenyl-H), 2.94-2.23 (m, 1H, p-cymene $CH(CH_3)_2$), 2.86 (s, 3H, p-cymene CH_3), 1.65–1.29 (d, J = 10.0 Hz, 6H, p-cymene $CH(CH_3)_2$). ^{13}C NMR (125 MHz, $CDCl_3$): δ, ppm 178.59 (C = Se), 158.84 (C = O), 137.17, 129.38, 128.66, 126.47, 122.82 (aromatic carbons), 112.91, 102.88, 98.90, 83.23, 82.33 (aromatic carbons of p-cymene), 31.25, 29.70, 18.42 (aliphatic carbons). LC-MS = 600.42 $[M]^+$.

Acknowledgments

The author Moideen Musthafa is thankful to MHRD, Govt. of India for providing senior research fellowship and Ramaiah Konakanchi, thanks the Malla Reddy Engineering College for Women (Autonomous Institution), Hyderabad, India, for support and encouragement during this research work.

Disclosure statement

No potential conflict of interest was reported by the authors.

References

Adeyemo, A. A., Shettar, A., Bhat, I. A., Kondaiah, P., & Mukherjee, P. S. (2018). Coordination-driven self-assembly of ruthenium(ii) architectures: Synthesis, characterization and cytotoxicity studies. *Dalton Transactions (Cambridge, England: 2003)*, *47*(25), 8466–8475. https://doi.org/10.1039/c8dt00962g

Alcolea, V., Plano, D., Karelia, D. N., Palop, J. A., Amin, S., Sanmartín, C., & Sharma, A. K. (2016). Novel seleno- and thio-urea derivatives with potent in vitro activities against several cancer cell lines. *European Journal of Medicinal Chemistry*, *113*, 134–144. https://doi.org/10.1016/j.ejmech.2016.02.042

Aneesrahman, K. N., Rohini, G., Bhuvanesh, N. S. P., Sundararaj, S., Musthafa, M., & Sreekanth, A. (2018). In vitro biomolecular interaction studies and cytotoxic activities of newly synthesised Copper(II) complexes bearing 2-hydroxynaphthaldehyde-based thiosemicarbazone. *Chemistry Select*, *3*(28), 8118–8130. https://doi.org/10.1002/slct.201800791

Balachandran, C., Haribabu, J., Jeyalakshmi, K., Bhuvanesh, N. S. P., Karvembu, R., Emi, N., & Awale, S. (2018). Nickel(II) bis(isatin thiosemicarbazone) complexes induced apoptosis through mitochondrial signaling pathway and G0/G1 cell cycle arrest in IM-9 cells. *Journal of Inorganic Biochemistry*, *182*, 208–221. https://doi.org/10.1016/j.jinorgbio.2018.02.014

Balakrishnan, N., Haribabu, J., Anantha Krishnan, D., Swaminathan, S., Mahendiran, D., Bhuvanesh, N. S. P., & Karvembu, R. (2019). Zinc(II) complexes of indole thiosemicarbazones: DNA/protein binding, molecular docking and in vitro cytotoxicity studies. *Polyhedron*, *170*, 188–201. https://doi.org/10.1016/j.poly.2019.05.039

Barbosa, F. A. R., Siminski, T., Canto, R. F. S., Almeida, G. M., Mota, N. S. R. S., Ourique, F., Pedrosa, R. C., & Braga, A. L. (2018). Novel pyrimidinic selenourea induces DNA damage, cell cycle arrest, and apoptosis in human breast carcinoma. *European Journal of Medicinal Chemistry*, *155*, 503–515. https://doi.org/10.1016/j.ejmech.2018.06.026

Bhat, M. A., Banoo, R., Rashid, H., Ashraf, A., Gul, S., Jameel, S., Butcher, R. J., & Lone, S. H. (2019). Synthesis, characterization, and theoretical studies of (E)-t-butyl-2-((E)-2-methyl-3-phenylallylidene) hydrazine carboxylate and (E)-t-butyl-2-((E)-3-phenylallylidene) hydrazine carboxylates as a possible Mcl-1 antagonists. *Journal of Molecular Structure*, *1181*, 197–202. https://doi.org/10.1016/j.molstruc.2018.12.061

Bhat, M. A., Lone, S. H., Ali, S., & Srivastava, S. K. (2018). Synthesis, spectral characterization, reactivity and DFT studies of novel ligand phenylseleno benzylacetate (L) and its complexes with group 12 metal chlorides. *Journal of Molecular Structure*, *1171*(L), 233–242. https://doi.org/10.1016/j.molstruc.2018.05.091

Bhat, M. A., Lone, S. H., & Srivastava, S. K. (2018). Synthesis, spectroscopic characterization, DFT studies and biological activity of bis (1-(ethyl) piperidine) diselenide (L) and its complexes with selected group 12 metal halides. *Inorganica Chimica Acta*, *478*, 222–231. https://doi.org/10.1016/j.ica.2018.04.011

Bratsos, I., Jedner, S., Gianferrara, T., & Alessio, E. (2007). Ruthenium anticancer compounds: Challenges and expectations. *CHIMIA International Journal for Chemistry*, *61*(11), 692–697. https://doi.org/10.2533/chimia.2007.692

Bruijnincx, P. C., & Sadler, P. J. (2008). New trends for metal complexes with anticancer activity. *Current Opinion in Chemical Biology*, *12*(2), 197–206. https://doi.org/10.1016/j.cbpa.2007.11.013

Burstein, E. A., Vedenkina, N. S., & Ivkova, M. N. (1973). Fluorescence and the location of tryptophan residues in protein molecules. *Photochemistry and Photobiology*, *18*(4), 263–279. https://doi.org/10.1111/j.1751-1097.1973.tb06422.x

Campos, J. C., Jr., Gouvêa, D. P., Ribeiro, C. S., Dutra, F. S. P., Stefanello, F. M., Pereira, C. M. P., Cunico W., Siqueira, G. M. (2018). Efficient synthesis and antioxidant evaluation of 2-aryl-3-(pyrimidin-2-yl)-thiazolidinones. *European* Journal of Medicinal Chemistry, *12*, 198–208. https://doi.org/10.1016/j.ejmech.2018.07.063

Costa, R. A., Pitt, P. O., Pinheiro, M. L. B., Oliveira, K. M. T., Salomé, K. S., Barison, A., & Costa, E. V. (2017). Spectroscopic investigation, vibrational assignments, HOMO-LUMO, NBO, MEP analysis and molecular docking studies of oxoaporphine alkaloid liriodenine. *Spectrochimica Acta Part A: Molecular and Biomolecular Spectroscopy*, *174*, 94–104. https://doi.org/10.1016/j.saa.2016.11.018

Coverdale, J., Laroiya-McCarron, T., & Romero-Canelón, I. (2019). Designing Ruthenium Anticancer Drugs: What Have We Learnt from the Key Drug Candidates? *Inorganics*, *7*(3), 31. https://doi.org/10.3390/inorganics7030031

Ganther, H. E. (1999). Selenium metabolism, selenoproteins and mechanisms of cancer prevention: Complexities with thioredoxin reductase. *Carcinogenesis*, *20*(9), 1657–1666. https://doi.org/10.1093/carcin/20.9.1657

Gopalakrishnan, D., Ganeshpandian, M., Loganathan, R., Bhuvanesh, N. S. P., Sabina, X. J., & Karthikeyan, J. (2017). Water soluble Ru(II)-arene complexes of the antidiabetic drug metformin: DNA and protein binding, molecular docking, cytotoxicity and apoptosis-inducing activity. *RSC Advances*, *7*(60), 37706–37719. https://doi.org/10.1039/C7RA06514K

Guerriero, A., Oberhauser, W., Riedel, T., Peruzzini, M., Dyson, P. J., & Gonsalvi, L. (2017). New class of half-sandwich ruthenium(II) arene complexes bearing the water-soluble CAP ligand as an in vitro anticancer agent. *Inorganic Chemistry*, *56*(10), 5514–5518. https://doi.org/10.1021/acs.inorgchem.7b00915

Harshitharaj, P. K., Kumar, R., & Ravi, S. (2016). Synthesis, cytotoxic activity and molecular docking study of bis-rhodanine derivative. *Journal of Chemical and Pharmaceutical Sciences*, *9*, 2478–2482.

Hill, J. M., & Speer, R. J. (1982). Organo-platinum complexes as antitumor agents (review). *Anticancer Research*, *2*(3), 173–186. Retrieved from http://europepmc.org/abstract/MED/6751211

Holben, D. H., & Smith, A. M. (1999). The diverse role of selenium within selenoproteins: A review. *Journal of the American Dietetic Association*, *99*(7), 836–843. https://doi.org/10.1016/S0002-8223(99)00198-4

Hussain, R. A., Badshah, A., Pezzuto, J. M., Ahmed, N., Kondratyuk, T. P., & Park, E. J. (2015). Ferrocene incorporated selenoureas as anticancer agents. *Journal of Photochemistry and Photobiology B: Biology*, *148*, 197–208. https://doi.org/10.1016/j.jphotobiol.2015.04.024

Hussain, R. A., Badshah, A., & Shah, A. (2014). Synthesis and biological applications of selenoureas. *Applied Organometallic Chemistry*, *28*(2), 61–73. https://doi.org/10.1002/aoc.3093

Jeyalakshmi, K., Haribabu, J., Balachandran, C., Bhuvanesh, N. S. P., Emi, N., & Karvembu, R. (2017). Synthesis of Ru(ii)-benzene complexes containing aroylthiourea ligands, and their binding with biomolecules and in vitro cytotoxicity through apoptosis. *New Journal of Chemistry*, *41*(7), 2672–2686. https://doi.org/10.1039/C6NJ03099H

Jeyalakshmi, K., Haribabu, J., Bhuvanesh, N. S. P., & Karvembu, R. (2016). Half-sandwich RuCl2(η(6)-p-cymene) core complexes containing sulfur donor aroylthiourea ligands: DNA and protein binding, DNA cleavage and cytotoxic studies. *Dalton Transactions (Cambridge, England: 2003)*, *45*(31), 12518–12531. https://doi.org/10.1039/c6dt01167e

Jeyalakshmi, K., Haribabu, J., Balachandran, C., Narmatha, E., Bhuvanesh, N. S. P., Aoki, S., Karvembu, R. (2019). Highly active copper(i) complexes of aroylthiourea ligands against cancer cells-synthetic and biological studies. *New Journal of Chemistry*, *43*, 3188–3198. https://doi.org/10.1039/c8nj04246b.

Konakanchi, R., Haribabu, J., Prashanth, J., Nishtala, V. B., Mallela, R., Manchala, S., Gandamalla, D., Karvembu, R., Reddy, B. V., Yellu, N. R., & Kotha, L. R. (2018). Synthesis, structural, biological evaluation, molecular docking and DFT studies of Co(II), Ni(II), Cu(II), Zn(II), Cd(II) and Hg(II) complexes bearing heterocyclic thiosemicarbazone ligand. *Applied Organometallic Chemistry*, *32*(8), e4415. https://doi.org/10.1002/aoc.4415

Konakanchi, R., Mallela, R., Guda, R., & Kotha, L. R. (2018). Synthesis, characterization, biological screening and molecular docking studies of 2-aminonicotinaldehyde (ANA) and its metal complexes. *Research on Chemical Intermediates*, *44*(1), 27–53. https://doi.org/10.1007/s11164-017-3089-y

Krishnamoorthy, P., Sathyadevi, P., Muthiah, P. T., & Dharmaraj, N. (2012). Nickel and cobalt complexes of benzoic acid (2-hydroxy-benzylidene)-hydrazide ligand: Synthesis, structure and comparative in vitro evaluations of biological perspectives. *RSC Advances*, *2*(32), 12190–12203. https://doi.org/10.1039/c2ra20597a

Kumar, V., Saravanan, P., Arvind, A., & Mohan, C. G. (2011). Identification of hotspot regions of MurB oxidoreductase enzyme using homology modeling, molecular dynamics and molecular docking techniques. *Journal of Molecular Modeling*, *17*(5), 939–953. https://doi.org/10.1007/s00894-010-0788-3

Lakowicz, J. R., & Weber, G. (1973). Quenching of fluorescence by oxygen. A probe for structural fluctuations in macromolecules. *Biochemistry*, *12*(21), 4161–4170. https://doi.org/10.1021/bi00745a020

Li, Y., Liu, Y., Wang, H., Xiong, X., Wei, P., & Li, F. (2013). Synthesis, crystal structure, vibration spectral, and DFT studies of 4-aminoantipyrine and its derivatives. *Molecules (Basel, Switzerland)*, *18*(1), 877–893. https://doi.org/10.3390/molecules18010877

Lone, S. H., Jameel, S., Bhat, M. A., Lone, R. A., Butcher, R. J., & Bhat, K. A. (2018). Synthesis of an unusual quinazoline alkaloid: Theoretical and experimental investigations of its structural, electronic, molecular and biological properties. *RSC Advances*, *8*(15), 8259–8268. https://doi.org/10.1039/C8RA00138C

Mahadevan, S., & Palaniandavar, M. (1998). Spectroscopic and voltammetric studies on copper complexes of 2,9-dimethyl-1,10-phenanthrolines bound to calf thymus DNA. *Inorganic Chemistry*, *37*(4), 693–700. https://doi.org/10.1021/ic961066r

Morris, G. M., Huey, R., Lindstrom, W., Sanner, M. F., Belew, R. K., Goodsell, D. S., & Olson, A. J. (2009). Reference-36 docking simulation.pdf. *Journal of Computational Chemistry*, *30*(16), 2785–2791. https://doi.org/10.1002/jcc.21256.AutoDock4 https://doi.org/10.1002/jcc.21256

Musthafa, M., Konakanchi, R., Ganguly, R., Pandikumar, P., & Sreekanth, A. (2020). Synthesis, characterization, *in silico* and *in vitro* biological activity studies of Ru(II) (*η6-p*-cymene) complexes with novel *N*-dibenzosuberene substituted aroyl selenourea exhibiting Se type coordination. *Research on Chemical Intermediates*, (Ii). https://doi.org/10.1007/s11164-020-04177-w

Muggia, F. (2009). Platinum compounds 30 years after the introduction of cisplatin: Implications for the treatment of ovarian cancer. *Gynecologic Oncology*, *112*(1), 275–281. https://doi.org/10.1016/j.ygyno.2008.09.034

Mukhopadhyay, S., Gupta, R. K., Paitandi, R. P., Rana, N. K., Sharma, G., Koch, B., Rana, L. K., Hundal, M. S., & Pandey, D. S. (2015). Synthesis, structure, DNA/protein binding, and anticancer activity of some half-sandwich cyclometalated Rh(III) and Ir(III) complexes. *Organometallics*, *34*(18), 4491–4506. https://doi.org/10.1021/acs.organomet.5b00475

Muralisankar, M., Bhuvanesh, N. S. P., & Sreekanth, A. (2016). Synthesis, X-ray crystal structure, DNA/protein binding and DNA cleavage studies of novel copper(ii) complexes of N-substituted isatin thiosemicarbazone ligands. *New Journal of Chemistry*, *40*(3), 2661–2679. https://doi.org/10.1039/C5NJ02806J

Musthafa, M., Aneesrahman, K. N., Perumalsamy, B., Ramasamy, T., Ganguly, R., & Sreekanth, A. (2019). Synthesis, crystal structure, DFT study, in vitro and in silico molecular docking of novel bis (aroyl selenourea) derivatives. *Journal of Molecular Structure*, *1180*, 585–594. https://doi.org/10.1016/j.molstruc.2018.12.019

Musthafa, M., Konakanchi, R., Ganguly, R., & Sreekanth, A. (2020). Novel dibenzosuberene substituted aroyl selenoureas: Synthesis, crystal structure, DFT, molecular docking and biological studies. *Phosphorus, Sulfur, and Silicon and the Related Elements*, *195*(4), 331–338. https://doi.org/10.1080/10426507.2019.1699924

Nikolić, S., Opsenica, D. M., Filipović, V., Dojčinović, B., Aranđelović, S., Radulović, S., & Grgurić-Šipka, S. (2015). Strong in vitro cytotoxic potential of new ruthenium-cymene complexes. *Organometallics*, *34*(14), 3464–3473. https://doi.org/10.1021/acs.organomet.5b00041

Olsen, J. I., Plata, G. B., Padrón, J. M., López, Ó., Bols, M., & Fernández-Bolaños, J. G. (2016). Selenoureido-iminosugars: A new family of multitarget drugs. *European Journal of Medicinal Chemistry*, *123*, 155–160. https://doi.org/10.1016/j.ejmech.2016.07.021

Pursuwani, B. H., Bhatt, B. S., Vaidya, F. U., Pathak, C., & Patel, M. N. (2020). Tetrazolo[1,5-a]quinoline moiety-based Os(IV) complexes: DNA binding/cleavage, bacteriostatic and photocytotoxicity assay. *Journal of Biomolecular Structure and Dynamics*, 1–10. https://doi.org/10.1080/07391102.2020.1756912

Ramachandran, E., Senthil Raja, D., Bhuvanesh, N. S. P., & Natarajan, K. (2012). Mixed ligand palladium(ii) complexes of 6-methoxy-2-oxo-1,2-dihydroquinoline-3-carbaldehyde 4N-substituted thiosemicarbazones with triphenylphosphine co-ligand: synthesis, crystal structure and biological properties. *Dalton Transactions (Cambridge, England : 2003)*, *41*(43), 13308–13323. https://doi.org/10.1039/c2dt31079a

Ramaiah, K., Srishailam, K., Laxma Reddy, K., Reddy, B. V., & Ramana Rao, G. (2019). Synthesis, crystal and molecular structure, and characterization of 2- ((2-aminopyridin-3-yl)methylene)-N-ethylhydrazinecarbothioamide using spectroscopic (^{1}H and ^{13}C NMR, FT-IR, FT-Raman, UV-Vis) and DFT methods and evaluation of its anticancer activity. *Journal of Molecular Structure*, 1184, 405–417. https://doi.org/10.1016/j.molstruc.2019.02.060

Ramakrishnan, S., & Palaniandavar, M. (2008). Interaction of rac-[Cu(diimine)3]2+ and rac-[Zn(diimine)3]2+ complexes with CT DNA: Effect of fluxional Cu(ii) geometry on DNA binding, ligand-promoted exciton coupling and prominent DNA cleavage. *Dalton Transactions*, *5*(29), 3866–3878. https://doi.org/10.1039/b801497c

Ramaiah, K., Prashanth, J., Haribabu, J., Srikanth, K. E., Venkatram Reddy, B., Karvembu, R., & Laxma Reddy, K. L (2019). Vibrational spectroscopic (FT-IR, FT-Raman), anti-inflammatory, docking and molecular characteristic studies of Ni(II) complex of 2-aminonicotinaldehyde using theoretical and experimental methods. *Journal of Molecular Structure*, *1175* (1175), 769–781. https://doi.org/10.1016/j.molstruc.2018.08.044

Konakanchi, R., Jyothi, P., & Kotha, L. R. (2019). Investigation of structures, FTIR, FT-Raman, in vivo anti-inflammatory, molecular docking and molecular characteristics of 2- amino-3-pyridine carboxaldehyde and its Copper(II) complex using experimental and theoretical approach. *Polycyclic Aromatic Compounds*, 1–23. https://doi.org/10.1080/10406638.2020.1725899

Reedijk, J. (2008). Metal-ligand exchange kinetics in platinum and ruthenium complexes: Significance for effectiveness as anticancer drugs. *Platinum Metals Review*, *52*(1), 2–11. https://doi.org/10.1595/147106708X255987

Rohini, G., Haribabu, J., Sheeba, M. M., K. N, A., Bhuvanesh, N. S. P., Balachandran, C., Karvembu, R., & Sreekanth, A. (2018). Ru(II)-$η$6-benzene complexes of dibenzosuberenyl appended aroyl/acylthiourea ligands: In vitro biomolecular interaction studies and catalytic transfer hydrogenation. *Chemistry Select*, *3*(1), 18–28. https://doi.org/10.1002/slct.201702538

Rohini, G., Ramaiah, K., Aneesrahman, K. N., Aryasenan, M. C., Bhuvanesh, N. S. P., Reddy, K. L., & Sreekanth, A. (2018). Biological evaluation, DNA/protein/binding aptitude of novel dibenzosuberene appended palladium(II)-thiourea complexes. *Applied Organometallic Chemistry*, *32*(12), e4567. https://doi.org/10.1002/aoc.4567

Rosenberg, B. (1978). Noble metal complexes in cancer chemotherapy. In G. N. Schrauzer (Ed.), *Inorganic and nutritional aspects of cancer* (pp. 129–150). Proceedings of the First Conference of the International Association of Bioinorganic Scientists, Inc. held in La Jolla, California, January 3–5, 1977. https://doi.org/10.1007/978-1-4684-0796-9-10

Sathyadevi, P., Krishnamoorthy, P., Butorac, R. R., Cowley, A. H., & Dharmaraj, N. (2012). Synthesis of novel heterobimetallic copper(i) hydrazone Schiff base complexes: A comparative study on the effect of heterocyclic hydrazides towards interaction with DNA/protein, free radical scavenging and cytotoxicity. *Metallomics: Integrated Biometal Science*, *4*(5), 498–511. https://doi.org/10.1039/c2mt00004k

Selvakumaran, N., Bhuvanesh, N. S. P., & Karvembu, R. (2014). Self-assembled Cu(ii) and Ni(ii) metallamacrocycles formed from 3,3,3′,3′-tetrabenzyl-1,1′-aroylbis(thiourea) ligands: DNA and protein binding studies, and cytotoxicity of trinuclear complexes. *Dalton Transactions (Cambridge, England : 2003)*, *43*(43), 16395–16410. https://doi.org/10.1039/c4dt01859a

Song, H. S., Song, Y. H., Singh, N., Kim, H., Jeon, H., Kim, I., Kang, S. C., & Chi, K.-W. (2019). New self-assembled supramolecular bowls as potent anticancer agents for human hepatocellular carcinoma. *Scientific Reports*, *9*(1), 1–13. https://doi.org/10.1038/s41598-018-36755-9

Swaminathan, S., Haribabu, J., Kalagatur, N. K., Konakanchi, R., Balakrishnan, N., Bhuvanesh, N., & Karvembu, R. (2019). Synthesis and anticancer activity of [RuCl2(η6-arene)(aroylthiourea)] complexes-high activity against the human neuroblastoma (IMR-32) cancer cell line. *ACS Omega*, *4*(4), 6245–6256. https://doi.org/10.1021/acsomega.9b00349